# Drug-induced changes in connectivity to midbrain dopamine cells revealed by rabies monosynaptic tracing

Katrina Bartas[1], May Hui[2], Pieter Derdeyn[1], Guilian Tian[2], Jose J. Vasquez[2], Ghalia Azouz[2], Cindy M. Yamamoto[2], Kevin T. Beier[2-5]

1 Program in Mathematical, Computational, and Systems Biology, University of California, Irvine, Irvine, CA, USA 92697-4560
2 Department of Physiology and Biophysics, University of California, Irvine, Irvine, CA, USA 92697-4560
3 Department of Neurobiology and Behavior, University of California, Irvine, Irvine, CA, USA 92697-4560
4 Department of Biomedical Engineering, University of California, Irvine, Irvine, CA, USA 92697-4560
5 Department of Pharmaceutical Sciences, University of California, Irvine, Irvine, CA, USA 92697-4560

*Corresponding author
Contact information:
Kevin Beier
825 Health Sciences Road
Medical Sciences D337
Irvine, CA 92697
Phone: 949-824-1083
Email: kbeier@uci.edu

**ABSTRACT:**

Drugs of abuse cause long-lasting changes in connectivity from inputs onto ventral tegmental area dopamine cells ($VTA^{DA}$) that contribute to drug-induced behavioral adaptations. However, it is not known which inputs are altered. Here we used a rabies virus-based mapping strategy to quantify rabies-labeled inputs to VTA cells after a single exposure to one of a variety of abused drugs – cocaine, amphetamine, methamphetamine, morphine, and nicotine – and compared the relative global input labeling across conditions. We observed that all tested drugs of abuse elicited similar input changes onto $VTA^{DA}$ cells, in particular onto DA cells projecting to the lateral shell of the nucleus accumbens and amygdala. In addition, repeated administration of ketamine/xylazine to induce anesthesia induces a change in inputs to $VTA^{DA}$ cells that is similar to but different from those elicited by a single exposure to drugs of abuse, suggesting that caution should be taken when using ketamine/xylazine-based anesthesia in rodents when assessing motivated behaviors. Furthermore, comparison of viral tracing data to an atlas of gene expression in the adult mouse brain showed that the basal expression patterns of several gene classes, especially calcium channels, were highly correlated with the extent of both addictive drug- or ketamine/xylazine-induced changes in rabies-labeled inputs to $VTA^{DA}$ cells. Reducing expression levels of the voltage-gated calcium channel *Cacna1e* in cells in the nucleus accumbens lateral shell reduced rabies-mediated input labeling of these cells into $VTA^{DA}$ cells. These results directly link genes controlling cellular excitability and the extent of input labeling by the rabies virus.

## INTRODUCTION:

The ventral tegmental area (VTA) contains dopamine cells ($VTA^{DA}$) that play key roles in several behavioral processes, including reward, aversion, and motor control[1–3]. $VTA^{DA}$ cells are heterogeneous, with recent studies identifying subpopulations of $VTA^{DA}$ cells that differentially contribute to adaptive and pathological behaviors[4–7]. Numerous studies have mapped the input-output architecture of VTA cells generally, as well as subpopulations of constituent DAergic, GABAergic, and glutamatergic cells[7–12]. These studies have helped us to understand the biased input and discrete output logic of the VTA, as well as generate hypotheses regarding the function of circuits including the VTA.

In addition to normal adaptive behaviors, $VTA^{DA}$ cells critically contribute to a variety of behaviors related to substance use disorder (SUD), including reward, sensitization, and withdrawal elicited by drugs of abuse[13–18]. For a variety of drugs of abuse, even a single exposure triggers long-lasting changes in synaptic plasticity onto $VTA^{DA}$ cells[19,20]. These changes include both a long-lasting enhancement of excitatory synaptic strength onto $VTA^{DA}$ cells[20], and development of inhibitory synaptic plasticity[21,22]. These changes are essential for a variety of drug-induced behaviors, linking plasticity at $VTA^{DA}$ cells with downstream behavioral changes[22–24]. Furthermore, the changes in excitatory synaptic plasticity specifically occur onto some cell types and not others[5], indicating that these adaptations are likely cell-type and pathway-specific. However, it remains unknown which sets of inputs are modified, and if these changes are consistent across abused drugs. Furthermore, synaptic plasticity is not the only type of long-lasting change that can be induced by drugs of abuse. Unfortunately, even less is known about how other forms of experience-dependent changes, including elevations in input activity, may contribute to addiction-related behaviors.

We recently showed that a single dose of cocaine causes long-lasting changes in cellular activity in inputs to $VTA^{DA}$ cells[15,16]. These changes occur from the globus pallidus external segment (GPe) and bed nucleus of the stria terminalis (BNST) projections to the VTA that contribute to drug-induced reward and sensitization, or withdrawal anxiety, respectively[15,25]. Notably, while these studies focused on inputs from the GPe and BNST, the viral mapping results also demonstrated the existence of other input changes to the VTA that were not pursued in those studies. These unexplored connections may provide critical information about how drugs alter connectivity onto $VTA^{DA}$ cells, which in turn contributes to drug-induced behavioral changes[15,16].

79 In this study, we explore the brain-wide changes in rabies-labeled inputs to VTA cells elicited by
80 a variety of different drugs, including drugs of abuse, an anesthetic mixture of ketamine/xylazine
81 (K/X), and fluoxetine, a psychoactive but non-abused control substance. Our study provides a
82 first-of-its-kind exploration into how even a single drug exposure can change brain-wide
83 connectivity patterns, in addition to highlighting some concerns about the potential effects of K/X
84 anesthesia on motivated behavior.
85
86 **MATERIALS AND METHODS:**
87 **Experimental Procedures**
88 Animals: Mice were housed on a 12-hour light–dark cycle with food and water ad libitum. Males
89 and females from a C57/BL6 background were used for all experiments in approximately equal
90 proportions. Mice were approximately 3-4 months of age at the time of experiments. All surgeries
91 were done under isoflurane or ketamine/xylazine anesthesia. All procedures complied with the
92 animal care standards set forth by the National Institute of Health and were approved by the
93 University of California, Irvine's Institutional Animal Care and Use Committee (IACUC).
94
95 Stereotaxic surgery: Mice were anesthetized with 3-4% isoflurane and maintained during surgery
96 at 1-1.5% isoflurane, or with a mixture of ketamine (100 mg/mL) and xylazine (5 mg/mL). Mice
97 were secured in a stereotaxic apparatus (Stoelting). Under aseptic conditions, guide holes were
98 drilled, and viruses were infused into the target sites using a glass capillary attached to a
99 microinjection pump (WPI, UMP3T). 100 nL of AAVs or 500 nL of EnvA-pseudotyped RABV were
100 infused at a rate of 1.6 nL/s. The glass capillary remained in place for 5 min following the infusion
101 to allow for virus diffusion. After infusion, the surgical incision sites were closed with either sutures
102 or Vetbond tissue adhesive (Patterson Veterinary). Vetameg (flunixin, Patterson veterinary) was
103 administered for pain management and topical bacitracin was applied to prevent infection at the
104 incision site.
105
106 For viral injections mapping experiments from a defined cell type, 100 nL of a 1:1 volume mixture
107 of $AAV_5$-CAG-FLEx$^{loxP}$-TCB and $AAV_8$-CAG-FLEx$^{loxP}$-RABV-G was injected into the VTA of DAT-
108 Cre[26], GAD2-Cre[27], or vGluT2-Cre mice[28]. Thirteen days later, animals were given a single
109 injection of a drug of abuse, fluoxetine, or saline. The following day, 500 nL of EnvA-pseudotyped
110 RABV was injected into the VTA. Animals were sacrificed five days later. For cTRIO experiments
111 shown in **Figure 4**, during the first surgery $AAV_5$-CAG-FLEx$^{FRT}$-TCB and $AAV_8$-CAG-FLEx$^{FRT}$-
112 RABV-G were injected into the VTA, and CAV2-FLEx$^{loxP}$-Flp was injected into an output site

113 (NAcLat, amygdala, NAcMed, mPFC) during the same surgery. All other procedures were the
114 same as above. RABV-labeled cells throughout the brain were manually quantified, as done
115 previously[7,10,15].
116
117 The injection coordinates and volumes used were as follows:
118 VTA: 100 nL AAV and 500 nL RABV, AP –3.2, LM 0.4, DV –4.2
119 NAcMed: 250 nL, AP +1.78, L0.4, DV –4.1
120 NAcLat: 250 nL, AP +1.45, LM 1.75, DV –4.0
121 Amygdala: 500 nL, AP –1.43, LM 2.5, DV –4.5
122 mPFC: 1 μL into mPFC (two injections of 500 nL, one at AP +2.15, LM 0.27, DV –2.1 and another
123 at AP +2.15, L0.27, DV –1.6
124
125 The titers of the viruses used, based on quantitative PCR analysis, were as follows:
126 $AAV_5$-CAG-FLEx$^{loxP}$-TC, 2.4 x $10^{13}$ genome copies (gc)/mL;
127 $AAV_8$-CAG-FLEx$^{loxP}$-G, 1.0 x $10^{12}$ gc/mL;
128 $AAV_5$-CAG-FLEx$^{FRT}$-TC, 2.6 x $10^{12}$ gc/mL;
129 $AAV_8$-CAG-FLEx$^{FRT}$-G, 1.3 x $10^{12}$ gc/mL;
130 CAV-FLEx$^{loxP}$-Flp, 5.0 x $10^{12}$ gc/mL.
131 The titer of RABVΔG was estimated to be 5.0 x $10^8$ colony forming units (cfu)/mL based on serial
132 dilutions of the virus stock followed by infection of the 293-TVA800 cell line.
133
134 Drug administration: Cocaine was administered (intraperitoneal injections) at a dose of 15 mg/kg,
135 morphine at 10 mg/kg, methamphetamine at 2 mg/kg, amphetamine at 10 mg/kg, nicotine at 0.5
136 mg/kg, and fluoxetine at 10 mg/kg.
137
138 Quantification of RABV data: RABV mapping data were analyzed as described previously[7,10]. All
139 RABV mapping data included were previously published[7,10,15], except for input tracing from mice
140 treated with a single dose of methamphetamine. A total of 118 samples were included in this study
141 (**Table 1**). Exclusion criteria included mice in which fewer than 200 input cells were labeled, or in
142 cases where injections were mistargeted (e.g., starter cells in the substantia nigra pars compacta).
143 Experimenters were blinded to the experimental condition when data quantification was being
144 performed. For starter cell center of mass calculations, we mapped the distribution of starter
145 neurons, as defined by TVA-mCherry expression along the A-P axis, and in the sections at the
146 center point along this axis, defined the center of labeling in along the M-L axis.

147

148 **CRISPRi experiments**

149 Plasmid construction: The CRISPRi system was adapted from Kumar's method[29]. pJEP317
150 pAAV-U6SaCas9gRNA(SapI)-EFS-GFP-KASH-pA was obtained from Addgene and was used as
151 a template to clone pJEP317-pAAV-U6-Cacna1eAC-EFS-GFP-KASH-pA using the Q5 Site-
152 directed mutagenesis kit (primers: 5'-acctccgtaaGTTTTAGTACTCTGGAAACAG-3' and 5'-
153 atgaacccttGGTGTTTCGTCCTTTCCAC-3') to insert the gRNA sequence
154 (AAGGGTTCATACCTCCGTAA) for *Cacna1e*. The gRNA sequence was selected from the IDT
155 Predesigned Alt-R™ CRISPR-Cas9 guide RNA resource
156 (https://www.idtdna.com/site/order/designtool/index/CRISPR_PREDESIGN). The plasmid for
157 CRISPRi (pJEP309-pAAV-EFS-dSaCas9-KRAB-Dio-pA), pAAV2-8, and pAAV2-5 were obtained
158 from Addgene. pHelper plasmid was a gift from Matthew Banghart at the University of California,
159 San Diego.

160

161 AAV production, purification, and titering: Generation of AAVs from plasmids and AAV Purification
162 by Iodixanol Gradient Ultracentrifugation were carried out as described on Addgene's
163 website with minor modifications. Briefly, pHelper, pAAV2-5/pAAV2-8 and pJEP309/pJEP317-
164 pAAV-U6-Cacna1eAC-EFS-GFP-KASH-pA plasmids were transfected into HEK293T cells using
165 PEIMAX (Polysciences, cat# 24765-100). The molar ratio for pHelper:pAAV2-5:transfer plasmid
166 was 1:1:1, and the ratio of total plasmids to PEIMAX was 1:3. 72 hrs post-transfection, cell lysate
167 and medium precipitated with PEG were purified by iodixanol gradient. Purified AAVs were titered
168 using primers against viral ITRs (5'-GGAACCCCTAGTGATGGAGTT-3' and 5'-
169 CGGCCTCAGTGAGCGA-3').

170

171 Viral injection: Prior to surgery, DAT-Cre mice were anesthetized with isoflurane (4% induction,
172 1-1.5% maintenance) and secured on a stereotaxic frame for precise localization of injection sites.
173 For assessment of *in vivo* genome editing, two conditions were generated. For the experimental
174 condition, 600 nL of a 1:1:1 volume mix of $AAV_8$-EFS-dSaCas9-KRAB-Dio, $AAV_9$-CamKII-0.4-
175 Cre-SV40 (Addgene, cat# 05558-AAV9) and $AAV_5$-U6-Cacna1eAC-EFS-GFP-KASH was
176 injected into the NAcLat. For a no gRNA control condition, 400 nL of a 1:1 volume mix of $AAV_8$-
177 EFS-dSaCas9-KRAB-Dio and $AAV_9$-CamKII-0.4-Cre-SV40 was infused into the NAcLat.

178

179 For mapping inputs to VTA cells in mice with *Cacna1e* downregulation in NAcLat, during a single
180 surgery, 300 nL of a of a 1:1 volume mix of $AAV_5$-FLEx$^{loxP}$-TC and $AAV_5$-FLEx$^{loxP}$-RABV-G was

181 injected into the VTA bilaterally, 600 nL of a 1:1:1 volume mix of $AAV_8$-EFS-dSaCas9-KRAB-Dio,
182 $AAV_9$-CamKII-0.4-Cre-SV40, and $AAV_5$-U6-Cacna1eAC-EFS-GFP-KASH was injected into the
183 left NAcLat, and 400 nL of a 1:1 volume mix of $AAV_8$-EFS-dSaCas9-KRAB-Dio and $AAV_9$-CamKII-
184 0.4-Cre-SV40 was injected into the right NAcLat. This study design enabled controls within the
185 same mice to prevent systematic biases due to differences in treatment of the mice. After 14 days,
186 RABVΔG was injected into the VTA. Mice were sacrificed five days later, and brains processed
187 as described below.
188
189 Brain section preparation, imaging, and cell counting: Five days after RABV injection, mice
190 underwent transcardial perfusion with 1x PBS followed by 4% formaldehyde in 1x PBS. Brains
191 were extracted and post-fixed in 4% formaldehyde for 24 hours, and then dehydrated with 30%
192 sucrose in 1x PBS. Brains were cut into 60 μm slices using a cryostat and mounted on Superfrost
193 Plus™ microscope slides (Fisher, cat # 1255015). Once the brain sections were fully dried on the
194 slide, they were rehydrated in 1xPBS containing DAPI at a dilution of 1:1000 (ThermoFisher, cat#
195 D1306). After 10 minutes, the liquid was removed, and Fluoromount-G (SouthernBiotech, cat#
196 0100-01) was applied to the sections. Coverslips (Thermo Scientific, cat# 152460) were used to
197 cover the brain sections on the slides. Images of the entire slides were captured using an Olympus
198 IX83 microscope, and manual cell counting was performed on the acquired images.
199
200 Determination of CRISPRi-mediated knockdown efficiency: To determine the efficacy of CRISPRi
201 knockdown of *Cacna1e* expression levels, 10 days following AAV injections into the NAcLat,
202 NAcLat brain tissue was dissected out from the brains of injected mice, and tissue was pooled (5
203 mice for *Cacna1e* gRNA and 3 mice for no gRNA control). Total RNA was extracted with TRIzol,
204 and 50 ng of total RNA was used for RT-qPCR using the Luna Universal One-Step RT-qPCR Kit
205 (New England Biolabs, cat# E3005L) following the manufacturer's
206 instructions. Phosphoglycerate Kinase 1 (PGK1) was used as the housekeeping gene for
207 normalization of *Cacna1e* mRNA levels.
208
209 **Dimensionality reduction of RABV input data**
210 For RABV input mapping experiments, quantified inputs cells were binned into 22 regions: Cortex
211 (anterior cortex), NAcMed, NAcLat, NAcCore, DStr, VP, PO, Septum, BNST, EAM, EP, GPe, PVH,
212 LHb, MHb, CeA, LH, ZI, DR, LDT, PBN, and DCN. Altogether, this dataset consists of the input
213 cell counts for these 22 regions across 118 mouse brains, with n=4 or 5 for each condition.
214

RABV input tracing data were reported as the percentage of total quantified labeled RABV inputs, as reported previously[7,10]. These data were further scaled using Z-score normalization. Principal Component Analysis (PCA) was then implemented on these normalized data using the scikit learn library in Python with default parameters[30]. Weights for PCA models were visualized as heatmaps, reflecting the contribution of each feature to each principal component. To test for differences between groups visualized in PC space, we assessed the value for each brain for each PC and if comparing 2 conditions, used an unpaired t-test, and if >2 conditions, a one-way ANOVA and if $p < 0.05$, followed by pairwise t-tests with multiple comparisons corrections (Dunnett or Tukey, as appropriate). Input values were the first 3 principal components, and significant differences between conditions for each principal component (drugs versus controls, for example) were denoted as having a p-value of less than 0.05. Results are reported where relevant in the text or in Table S2.

Uniform Manifold Approximation and Projection (UMAP), implemented using the UMAP library in Python, was used to generate alternative visualizations of the RABV input data[31]. To choose and standardize our UMAP parameters across analyses, we investigated which methods placed mouse brains of the same type and treatment close together most consistently. For the distance metric parameter, the metrics we found to perform best were Euclidean and cosine, but we chose to use the Euclidean metric for consistency with previous analyses[32]. For the number of neighbors parameter, we chose a large number, ⅓ the size of each of our datasets, for a more global view of the data. Other parameters were kept at the default values. To account for the stochasticity of individual embeddings, we applied UMAP 20 times to each data set and found the results to be very similar, as found in previous analyses[32]. The results were then presented as correlograms. Clustered heatmaps and plots of these data were made using a combination of the Python packages seaborn[33] and matplotlib[34]. The seaborn clustermap function was implemented with default values, including Euclidean distance as the distance metric.

To better visualize the distribution of a given condition in PCA and UMAP space, we overlaid the points with ellipsoids. Ellipsoids were centered at the average coordinate of a condition and stretched one standard deviation along the primary and secondary axes.

**Brain Region Selection in the Allen Mouse Brain Atlas**

To compare our data with connectivity data from the Allen Institute, we converted our 22 brain regions into regions or groups of regions defined by the Allen Atlas. This was necessary as our

249 region annotations defined while doing cell counts of the RABV data were at times different from
250 the Allen Mouse Brain Atlas-defined regions. 22 brain regions were used for RABV analyses, but
251 these were reduced to 20 brain regions (NAcMed, NAcLat, and NAcCore were merged into the
252 NAc) for comparison with Allen Atlas data. In several cases, multiple Allen-defined regions were
253 used to constitute a single region that we defined, as in the case of the cortex. A summary of
254 these conversions is as follows:

| Full brain region name | Standard abbreviation | Allen abbreviations |
|---|---|---|
| Cortex | Anterior cortex | PL, ILA, ORB, GU, AI, MOs, MOp |
| Nucleus accumbens (medial) | NAcMed | ACB |
| Nucleus accumbens (lateral) | NAcLat | ACB |
| Nucleus accumbens (core) | NAcCore | ACB |
| Dorsal striatum | DStr | STRd |
| Ventral pallidum | VP | PALv |
| Preoptic area | PO | MPO, LPO |
| Septum | Septum | LSX, MS |
| Bed nucleus of the stria terminalis | BNST | BST |
| Extended amygdala area | EAM | MEA, AAA, NLOT, COA, MA, BMA, EPv, NDB |
| Internal globus pallidus | EP | GPi |
| External globus pallidus | GPe | GPe |
| Paraventricular nucleus of the hypothalamus | PVH | PVH |
| Lateral habenula | LHb | LH |
| Medial habenula | MHb | MH |
| Central nucleus of the amygdala | CeA | CEA |
| Lateral hypothalamus | LH | LHA |
| Zona incerta | ZI | ZI |
| Dorsal raphe nucleus | DR | DR, PAG |

| | | |
|---|---|---|
| Laterodorsal tegmental nucleus | LDT | LDT |
| Parabrachial nucleus | PBN | PB |
| Deep cerebellar nuclei | DCN | CBN |

255

256 **Allen Mouse Brain Connectivity Atlas projection portrait construction**

257 Projection portraits of the VTA were made using data from the Allen Mouse Brain Connectivity
258 Atlas[35], as described previously[32]. Briefly, data from 20 input brain regions, as defined in the
259 above table, were downloaded and used for analyses. Cre-based and non-Cre-based
260 experiments representative of each brain region were chosen for visualization. Labeled cell
261 bodies at the site of injection often spread into adjacent brain regions or only covered a part of a
262 region. Several experiments were chosen to account for this variation and give a better estimate
263 for each region's projections. Experiment IDs are recorded in Table S1 in our previous work[32].
264 Connectivity of brain regions of interest to the VTA was visualized by showing a representative
265 slice of the VTA and coloring the image based on high or low connectivity according to averaged
266 AAV tracing data. AAV tracing data were averaged across experiments and across brain regions
267 that grouped together according to weights assigned by PCA, as shown in **Figures 1, 3, and 4**.

268

269 Data for projection portraits and for subsequent network construction was accessed using the
270 python Allen SDK package, developed and maintained by the Allen Institute for Brain Science.

271

272 **Gene Expression Data Access and Processing**

273 Gene expression data was downloaded from the Allen Institute's Anatomic Gene Expression Atlas
274 (AGEA)[36], an *in situ* hybridization dataset which has annotated expression of 19,932 genes to
275 every brain region defined in the Allen Mouse Brain Atlas. We used code written by Eli Cornblath
276 (https://github.com/ejcorn/mouse_abi_tool) to access and download gene expression data for our
277 regions of interest, as done in a previous study[37]. To ensure only high-quality data were included
278 in our analyses, we filtered experiments based on metrics used in previous analyses of this
279 dataset[38]. We retained genes for which there were data from coronal sections, or where the
280 Pearson correlation coefficient across experiments was over 0.5 for a particular gene in our
281 regions of interest. This filtering left us with 4,283 unique genes for the 36 Allen-defined brain
282 regions to be aggregated to compare with our 22 quantified input sites from the RABV mapping
283 data. We averaged data among brain regions that were defined differently in the atlas versus our
284 RABV quantifications, which resulted in a total of 20 brain regions for comparative analyses, as

detailed above. Data were normalized using a scaled sigmoid function, a method that is robust to outliers and was used in previous analyses of these data[39].

**Gene expression data analysis and comparison to RABV data**

To investigate how basal gene expression might be correlated to connectivity changes after drug exposure, we used processed data from the AGEA. For each experimental condition, the RABV data for the drug-treated animals were compared to those of the saline-treated controls. To quantify this comparison, we computed a ratio, as used in **Figures 6 and S7-9**, by dividing the average RABV counts in each brain region for the experimental condition by the average RABV counts in each brain region for the saline condition. This resulted in a vector of 22 ratios for each experimental condition, one ratio for each brain region. We also computed a difference, as used in **Figures 5 and S4-S6**, by subtracting the average RABV counts in each brain region for the experimental condition by the average RABV counts in each brain region for the saline control condition. This resulted in a vector of 22 differences for each drug comparison, one difference for each brain region.

We calculated the correlation of the condition-control differences with gene expression data for each region. The Spearman correlation coefficient between the gene expression across regions and our RABV differences was used because the correlative relationship between these values cannot be assumed to be linear. A similar method was used in previous analyses[38]. A high positive correlation between a gene and an experimental condition ratio was interpreted as a greater likelihood of a brain region to exhibit RABV labeling changes after drug exposure if this gene is highly expressed before drug exposure. A negative correlation between a gene and an experimental condition ratio was taken to mean this region would be more likely to exhibit RABV labeling changes after drug exposure if the gene expression level is low.

We performed GO analysis on the top 50 most highly correlated genes and on the top 50 most negatively correlated genes. GO analysis was performed using the EnrichR package[40]. Lists of genes with highly positive or negative correlations to our condition differences were compared to GO annotations using the coding language R. The 2021 version of two databases were queried: GO Biological Process and GO Molecular Function. GO enrichment analysis results were visualized in dot plots using the package ggplot2, as shown in **Figures 5 and S4-S6**.

318 We next compared the drug/isoflurane ratios for a group of addictive drugs to gene expression of
319 subsets of genes of interest (**Figure 6, S7**). Similar analyses were done for ketamine and
320 fluoxetine (**Figure S8, S9**). The subgroups of genes used were synapse-related genes[41], ion-
321 channel related gene[42], neurotransmitter receptor-related genes[43], differentially expressed genes
322 related to substance dependence GWAS[44], and exo- and endocytosis-related genes[45]. Other
323 subsets of genes of interest were defined using the Guide to Pharmacology database[46].
324 Correlation coefficients (Spearman's ρ) and p-values are reported in the figures.
325
326 **RESULTS:**
327 **Dimensionality reduction methods identify differences in inputs of VTA cell populations**
328 We and others previously showed that DAergic, GABAergic, and glutamatergic cells in the VTA
329 receive inputs from similar brain regions, with some quantitative differences that varied depending
330 on the study[10,12]. In our work we also showed that connectivity differences in the VTA are largely
331 a consequence of spatial organization of cells within the VTA[7,10,32]. The fact that the distributions
332 of these three VTA cell populations are largely spatially overlapping may explain why the global
333 inputs to each population are similar. However, one limitation in interpreting these studies is that
334 they focused on individual comparisons of input counts on a per region basis. While this is a
335 common approach in analyzing viral tracing data, and useful for both hypothesis generation and
336 testing, it fails to account for the higher-level organization of input patterns. Our goal here is to go
337 beyond considering single brain regions and better understand the holistic connectivity patterns
338 of different cell populations or drug treatment conditions.
339
340 Our first goal was to explore the potential differences in input patterns generated using RABV
341 tracing to each of the DAergic, GABAergic, and glutamatergic neuron populations in the VTA
342 using principal component analysis, PCA. A schematic of the experiment is shown in **Figure 1A**,
343 with representative images of brain regions of interest in **Figure 1B**. A standard representation of
344 these data, a bar plot, is shown in **Figure 1C**. PCA embedding resulted in the three cell
345 populations clustering into largely distinct groups (**Figure 1E**). We considered the first two
346 principal components (PCs), which explain the most variance in the data. In PC space, DAT-Cre
347 brains were characterized by low PC1 and low PC2 values, GAD2-Cre brains by high PC1 values,
348 and vGluT2-Cre brains by high PC2 values. The differences we noted were statistically significant:
349 PC1 values of GAD2-Cre compared to DAT-Cre brains were significantly different (One-way
350 ANOVA $p = 0.010$, DAT-Cre vs. GAD2-Cre multiple comparisons adjusted $p = 0.0087$; **Figure 1F**)
351 and PC2 values of DAT-Cre compared to vGluT2-Cre brains were significantly different (One-way

352 ANOVA p = 0.016, DAT-Cre vs. vGluT2-Cre multiple comparisons adjusted p = 0.016; **Figure**
353 **1G**). An advantage of PCA over other dimensionality reduction approaches is that, because it is
354 a linear approach, the weights of each feature's contribution to each PC can be clearly interpreted.
355 In this case, we can infer which brain regions contribute most to the positive and negative
356 dimensions of each PC. For example, in our data, DAT-Cre and GAD2-Cre brains were separated
357 along PC1. Brain regions that contributed to the positive dimension of PC1 were the BNST,
358 entopeduncular nucleus (EP), GPe, central amygdala (CeA), and zona incerta (ZI) (**Figure 1D**).
359 These inputs were enriched onto GABAergic cells relative to DA cells (**Figure 1C**). To identify
360 where in the VTA these input populations projected, we assembled projection portraits of these
361 inputs to the VTA as we did previously[32]. This approach uses axonal projection data available
362 from the Allen Mouse Brain Connectivity Atlas to generate spatial heatmaps that show "hotspots"
363 of innervation in the midbrain[35]. We first selected experiments where GFP was expressed in the
364 input regions of interest. Pixel values representing projection density were pulled from a
365 representative coronal slice containing the VTA for each region. For a given set of inputs of
366 interest, we averaged together their projections to the VTA to see if the group had any common
367 spatial trends (**Figure 1H**). The projection portrait of the positive PC1 inputs indicated that they
368 preferentially project dorsally and laterally to areas surrounding the VTA (**Figure 1I**). In contrast,
369 the regions that contributed most strongly to the negative dimension of PC1 were the anterior
370 cortex, nucleus accumbens medial shell (NAcMed), ventral pallidum (VP), preoptic area (PO),
371 septum, lateral habenula (LHb), medial habenula (MHb), and lateral hypothalamus (LH). These
372 inputs were more highly labeled in DAT-Cre mice. The projection portrait of these inputs highlights
373 the whole VTA and not surrounding regions (**Figure 1J**). While the distribution of starter cells in
374 the VTA in DAT-Cre and GAD2-Cre mice is spatially overlapping[7], this analysis indicates that
375 inputs with biases onto DA cells target the VTA itself while those biased onto GABAergic cells
376 preferentially target areas dorsal and lateral to the VTA.
377
378 While DAT-Cre and GAD2-Cre conditions were separated along PC1, DAT-Cre and vGluT2-Cre
379 conditions were separated along PC2. Regions that contributed to the positive dimension of PC2
380 included the LHb, MHb, EP, ZI, and deep cerebellar nuclei (DCN) as well as the cortex, while
381 those contributing to the negative dimension included the NAcMed, nucleus accumbens lateral
382 shell (NAcLat), nucleus accumbens core (NAcCore), dorsal striatum (DStr), and GPe (**Figure 1K-**
383 **L**). The MHb and LHb both project medially in the VTA, whereas the NAcMed, NAcLat, NAcCore,
384 DStr, and GPe all project laterally[32]. The projection portrait corresponding to the positive
385 dimension of PC2 highlights the area dorsal of the VTA, as well as the medial aspect of the VTA

386 (**Figure 1K**), while those corresponding to the negative dimension highlight the ventrolateral
387 aspect of the ventral midbrain, including the substantia nigra pars reticulata (SNr) (**Figure 1L**).
388 These results are consistent with the medial-lateral projection gradient that principally divides the
389 projections into the VTA, with inputs from the basal ganglia projecting to the lateral portion of the
390 VTA and the habenula projecting to the medial portion[32]. As inputs from the MHb and LHb
391 contribute positive weights to the PC2 axis and vGluT2-Cre brains have the most positive PC2
392 values, it suggests that most of the vGluT2-expressing cells in the VTA are located within the
393 medial portion of the VTA. This is consistent with previous reports using immunohistochemistry
394 and in situ hybridization[47,48]. In addition, the EP, ZI, and DCN all project predominantly to the red
395 nucleus, and the cortex also innervates the red nucleus, which contains glutamatergic neurons
396 and is located dorsal to the VTA (**Figure 1K**). While injections for our viral mapping studies
397 targeted the VTA and most starter neurons were within the VTA, there were some starter neurons
398 in vGluT2-Cre brains located in the red nucleus. In contrast, this was not the case in DAT-Cre
399 brains[10]. As these starter populations were also largely spatially overlapping, the data indicate
400 that inputs with biases onto glutamatergic cells target the dorsomedial aspect of the VTA, while
401 those with a relative bias onto DA cells preferentially target the ventrolateral aspect of the VTA.
402
403 While PCA is particularly useful due to the interpretability of the weights of the PCs, it cannot
404 capture non-linear relationships in high-dimensional data, which are common in complex systems
405 like in neuroscience. To examine the overall relationship of input patterns between DAT-Cre,
406 GAD2-Cre, and vGluT2-Cre cell populations, we performed a second analysis on inputs from
407 each population using Uniform Manifold Approximation and Projection, UMAP, which can capture
408 more complex relationships than PCA. We found that DAT-Cre and GAD2-Cre brains were the
409 most separated in UMAP space, with vGluT2-Cre brains located between them (**Figure 1M**). This
410 is consistent with the overlap in neurotransmitters released by these cells: cells expressing DA
411 markers such as tyrosine hydroxylase (TH) and traditional GABAergic markers such as GAD2 are
412 nearly mutually exclusive, while there is considerable overlap between cells expressing DA
413 markers and glutamatergic markers, as well as cells expressing GABAergic markers and
414 glutamatergic markers[10,12,49–51]. Note that while DA neurons have been found to co-transmit DA
415 and GABA[52,53], this occurs through a non-canonical GABA synthesis pathway, and therefore DA
416 cells do not express typical markers of GABAergic cells, such as GAD2, used to define the Cre
417 line in our study.
418

419 Since individual UMAP embeddings are stochastic depending on initial seeding conditions, we
420 examined the average Euclidian distance between pairs of brains in 20 UMAP embeddings and
421 plotted the averaged results as a correlogram. This showed that DAT-Cre and vGluT2-Cre brains
422 were more like one another, and the GAD2-Cre brains were the most distinct from the other
423 conditions (**Figure 1N**). These results are thus consistent with the known neurochemical overlap
424 between these cells and indicate that DAT-Cre and vGluT2-Cre label more overlapping cells with
425 each other than with GAD2-Cre. In sum, these results serve to demonstrate that we can
426 recapitulate the locations of different neurochemically-defined cells in the VTA based on PCA and
427 projection portraits based on information from RABV input mapping data. They also provide a
428 validation of our approach for dissecting the relationships between input patterns and different
429 cell types within the VTA, as the conclusions about the relationship between input regions and
430 cell types agree with other studies using different, complementary methodologies.
431
432 **A single injection of a drug of abuse changes brain-wide input patterns to VTA$^{DA}$ cells**
433 With our dimensionality reduction approaches validated on our cell type-specific RABV data, we
434 next applied them to examining how drugs of abuse may alter VTA input patterns. We first
435 assessed whether the psychoactive but non-addictive fluoxetine altered brain-wide input patterns
436 relative to saline-injected mice. We found no clear differences in inputs between these conditions,
437 and they overlapped completely in PC space – with no significant differences between PC1, PC2,
438 or PC3 between the saline and the fluoxetine brains ($p > 0.05$ for PC1-3) - indicating fluoxetine
439 did not alter brain-wide input patterns to VTA$^{DA}$ cells (**Figure 2A-F**). We therefore combined these
440 groups for additional statistical power and tested whether a single administration of one of several
441 drugs of abuse caused changes in brain-wide input patterns to VTA$^{DA}$ cells, first considered as a
442 single group. When comparing combined controls to the drugs group, we observed a statistically
443 significant difference in input patterns, including a reduction in inputs from the DStr and elevation
444 in inputs from the GPe following drug injection (**Figure 2G**). In order to more fully assess which
445 input sites may differentiate the control- versus drug-treated groups, we again used PCA. We
446 observed separation between the control and drug groups principally along PC2, with no
447 separation along PC1 and minimal separation along PC3 (**Figure 2H-I**). These differences in PC
448 space were statistically significant: as we observed visually, the control group's PC2 and PC3
449 values were significantly different from the drug group's PC2 and PC3 values ($p = 0.0009$ and $p$
450 $= 0.024$ for PC2 and PC3, respectively; **Figure 2K-L**). There was no significant difference
451 between drugs and controls in PC1 ($p = 0.78$; **Figure 2J**). The positive axis of PC2, which was
452 enriched in drug-treated brains, was driven by inputs from EAM, EP, GPe, LH, and PBN, while

453 the negative axis was driven by the NAcMed, NAcCore, DStr, septum, and MHb (**Figure 2M**).
454 Notably, the most negative weights for PC2, namely the NAcMed, NAcCore, DStr, septum, and
455 MHb are all reduced in drug-treated brains (**Figure 2G**). Conversely, the most positive weights,
456 namely the EAM, EP, GPe, LH, and PBN, are all increased in drug-treated brains (**Figure 2G**).
457 Therefore, while PCA allows us to observe trends consistent with traditional methods, we can
458 also observe the relationship between the percentage of inputs among different brains, and also
459 identify relationships that are not immediately apparent in the data when presented as bar graphs.
460 For example, while the BNST, CeA, and ZI do not show clear differences in control vs. drug-
461 treated brains in the bar graphs, they are all positive weights in PC2 and thus, likely change in
462 concert with regions such as the GPe and PBN (**Figure 2G-M**).
463
464 Importantly, unlike traditional bar graph approaches, PCA allows us to isolate technical variation
465 from the experiments, enabling us to focus more clearly on changes induced by the relevant
466 variable, here treatment with a control substance or drug of abuse. For example, PC1 does not
467 distinguish control vs. drug-treated brains (**Figure 2H, J**), indicating this variable was inherent to
468 the way the experiment was performed and not related to drug or control treatment. The strongest
469 negative weights for PC1 were the NAcLat, NAcCore, DStr, and GPe, while the strongest positive
470 weights for PC1 were the VP, PO, LHb, and DR (**Figure 2M**). This is consistent with connectivity
471 differences along the medial-lateral axis of the VTA, which underlies many of the connectivity
472 differences to different $VTA^{DA}$ subpopulations[7,10,32]. To assess whether PC1 may reflect
473 differences the location of starter cells in the VTA, we first assessed whether there was a
474 systematic difference in starter cell location between conditions. We noted a high level of overlap
475 in starter cell distribution between conditions (**Figure 2N**), indicating that this alone likely did not
476 explain differences between control and drug-treated groups. We then assessed whether brain to
477 brain variation in starter cell distribution could explain the effects observed along PC1. We
478 therefore colored each point in PC space according to the assessed center of injection for each
479 experiment. We noted a clear medial-lateral gradient along PC1, but not PC2 or PC3 (**Figure 2O-**
480 **P**). To test the significance of this relationship, we performed linear regression analysis,
481 comparing the x-coordinate of the injection center relative to location along PC1, PC2, or PC3 for
482 each brain. We observed a highly significant positive correlation with PC1, a slightly positive but
483 non-significant correlation with PC2, and no correlation for PC3 (**Figure 2Q-S**). These results
484 show that PC1 reflects variation in the injection site within the VTA, while PC2 reflects changes
485 induced by drugs of abuse, allowing us to isolate the changes in input connectivity induced by
486 administration of a single drug of abuse.

487

488 With our integrative methodology validated on cell type specific RABV data and demonstrating
489 that drugs of abuse alter brain-wide input patterns to $VTA^{DA}$ cells, we applied our approaches to
490 explore the effects of each drug specifically, as well as potential effects of the 2x use of the K/X
491 anesthetic mixture. We first asked two questions: 1) How do injections of different drugs of abuse
492 change the connectivity patterns onto VTA cells? 2) How do these potential drug-induced
493 differences relate to differences between unique cell types in the VTA? To answer these, we first
494 assessed experiments with ten separate experimental conditions: 2 conditions of GAD2-Cre mice,
495 and 8 conditions of DAT-Cre mice. The GAD2-Cre mice were all anesthetized with isoflurane and
496 administered either saline or cocaine one day prior to RABV injection. The DAT-Cre mice were
497 given either isoflurane or K/X-based anesthesia. The K/X-anesthetized mice were administered
498 saline. The isoflurane anesthetized mice were administered either saline, fluoxetine,
499 amphetamine, cocaine, methamphetamine, morphine, or nicotine. RABV mapping was performed
500 from targeted VTA cells in all cases, and the brain-wide inputs were quantified. We then performed
501 PCA on the combined RABV tracing datasets, which showed that brains from GAD2-Cre mice
502 were in the positive dimension of PC1, while those from DAT-Cre mice were in the negative
503 dimension (**Figure 3A**), regardless of the substance administered. This difference in PC1 was
504 highly statistically significant (One-way ANOVA $p < 0.0001$; all conditions pairwise comparisons
505 with GAD2-Cre, multiple comparisons adjusted $p < 0.0001$; **Figure 3B**). The positive dimension
506 of PC1 received contributions from largely the same sets of regions as in the previous analysis of
507 DAT-Cre, GAD2-Cre, and vGluT2-Cre brains, which included the BNST, EP, ZI, CeA, as well as
508 the DCN (**Figure 3H, 1D**). Given that the same set of brain regions differentiated DAT-Cre and
509 GAD2-Cre brains along PC1 in both datasets, this suggests that the intrinsic differences in inputs
510 to different cell populations in the VTA are more pronounced than differences induced by drugs
511 of abuse, fluoxetine, or the method of anesthesia. Notably, these patterns were unlikely to be
512 obtained by chance; scrambling the sample identity and percentage of RABV-labeled cells in each
513 input site resulted in groups that overlapped in both PCA and UMAP space (**Figure S1**).
514

515 To specifically explore potential drug-induced differences in input labeling onto $VTA^{DA}$ cells, we
516 removed GAD2-Cre brains from the dataset. Results and representative images are shown in
517 **Figure 3J-K**. In PCA analyses of these brains only, PC1 and PC3 largely failed to differentiate
518 the conditions, with no significant differences observed (**Figure 3C-G**), while PC2 significantly
519 differentiated the conditions (One-way ANOVA $p = 0.0093$; saline vs. drugs multiple comparisons
520 adjusted $p = 0.034$; **Figure 3F**). The most negative weights to PC1 were contributed by the basal

521 ganglia inputs that project to the SNr, located ventrolaterally to the VTA (**Figure 3I, L**) while
522 positive contributors came from brain regions that projected more medially (LHb, MHb, dorsal
523 raphe (DR)) and centrally to the VTA (ventral pallidum (VP), PO, extended amygdala area (EAM),
524 paraventricular nucleus of the hypothalamus (PVH), and LH) (**Figure 3I, M**). This is consistent
525 with a gradient along the medial-lateral axis[32]. As it did not differentiate the conditions, this axis
526 likely represents experimental variations in the location of starter cell populations within the
527 VTA[7,10,32]. The regions with the largest positive contribution to PC2 included the EAM,
528 parabrachial nucleus (PBN), DR, EP, and LH, with lesser contributions from the GPe, DCN, ZI,
529 CeA, and BNST (**Figure 3I, N**). These regions were over-represented in animals treated with a
530 single administration of a drug of abuse. Notably, this group of inputs contains brain regions that
531 are involved in the brain's stress response such as the PBN, EAM, CeA, and BNST, and have
532 been implicated in drug-induced behaviors[54,55]. For example, we recently showed the importance
533 of the GPe in conditioned place preference and locomotor sensitization and the BNST in drug-
534 induced withdrawal[15,25]. The regions with the largest negative contribution to PC2 included the
535 NAcMed, NAcCore, DStr, Septum, and MHb (**Figure 3I, O**). These regions were
536 underrepresented in animals given a single administration of a drug of abuse. These results
537 together demonstrate that drugs of abuse cause long-lasting changes in input populations to DA
538 cells, and that we can identify which sets of inputs distinguish drug-treated vs. control-treated
539 brains. These changes may be functionally important, as we previously demonstrated the
540 functional role of two inputs that we identified as differing between drug-treated and control
541 conditions.
542
543 Lastly, we wanted to explore the overall relationship between input changes induced by different
544 drugs. As before, we used UMAP to explore the higher-level organization of these conditions to
545 compare the relationship of holistic input patterns between groups. We found that the mice
546 anesthetized with isoflurane and treated with saline overlapped with the isoflurane-anesthetized,
547 fluoxetine-treated group, but not the K/X-anesthetized and saline-treated group (**Figure 3P**).
548 These conditions were segregated from animals treated with the drugs of abuse -
549 psychostimulants, morphine, and nicotine. Our analysis of the relationships between individual
550 conditions, generated using the Euclidian distances between points in 20 UMAP embeddings as
551 before, demonstrated that the expected control conditions formed a cluster (saline, fluoxetine)
552 distinct from the other groups. Interestingly, the K/X-anesthetized animals were more closely
553 associated with the mice treated with addictive drugs, in particular morphine, than with controls
554 (**Figure 3Q**). This suggests that drugs of abuse cause similar changes in brain-wide input patterns

555 to one another in DAT-Cre mice, and that input patterns in K/X-anesthetized animals more closely
556 resemble morphine-treated mice than saline-treated mice. This indicates that the method of
557 anesthesia, either using isoflurane or K/X, results in different patterns of input labeling. Given the
558 similarity of input patterns in K/X-anesthetized mice to isoflurane-anesthetized mice treated with
559 a drug of abuse but not saline, we suspect that two doses of K/X-anesthesia as is required for
560 RABV circuit mapping experiments triggers changes in input patterns in rodent brains that last at
561 least the five-day duration of these experiments.
562
563 **Anesthetic doses of K/X cause long-lasting changes in inputs to VTA$^{DA}$→NAcLat and**
564 **VTA$^{DA}$→Amygdala cells**
565 To examine how differences in anesthesia methods may impact brain-wide input patterns, we
566 performed some more targeted comparisons. When comparing only two groups using PCA –
567 isoflurane-anesthetized animals to K/X-anesthetized animals – these conditions completely
568 segregated (**Figure 4A**). While the difference in PC1 was not quite significant ($p = 0.086$), the
569 difference in PC2 was significant ($p = 0.037$). This separation was driven by positive weights from
570 the VP, PO, EAM, PVH, LH, and PBN along PC1, which were more strongly represented in the
571 K/X-anesthetized mice and whose combined projection portrait broadly targets the VTA (**Figure**
572 **4A, C, P, U**), and the NAcLat, DStr, GPe, and PVH along PC2, which were also more strongly
573 represented in the K/X-anesthetized mice whose combined projection portrait targets
574 ventrolateral to the VTA (**Figure 4A, C, P, V**). A similar separation of conditions was observed
575 using UMAP (**Figure 4B**).
576
577 Next, we wanted to assess which VTA$^{DA}$ cells may be impacted by whether the animals received
578 isoflurane or K/X-based anesthesia. To test this, we performed cell type-specific Tracing of the
579 Relationship between Inputs and Outputs (cTRIO) for each of four different VTA$^{DA}$ subpopulations:
580 those projecting to the NAcMed, NAcLat, amygdala, or mPFC, and receiving K/X anesthesia and
581 saline, isoflurane and saline, or isoflurane and cocaine. The differences in input patterns between
582 conditions were most pronounced for VTA$^{DA}$→NAcLat cells, where the isoflurane- and K/X-treated
583 groups segregated, both in PCA and UMAP space (**Figure 4D-F**). Groups appeared to differ along
584 both PC1 and PC2, though differences in PC2 were not statistically significantly different, with
585 K/X-treated brains being characterized by lower PC1 values which received contributions
586 principally from the anterior cortex, NAcMed, NAcLat, NAcCore, septum, PVH, and MHb, as well
587 as higher PC2 values which received contributions from the VP, PO, EAM, LHb, and LH (PC1,
588 One-way ANOVA $p = 0.0003$, saline vs. cocaine multiple comparisons adjusted $p = 0.011$, k/x vs.

589 cocaine multiple comparisons adjusted p = 0.0002; **Figure 4D, Q, W, X**). The following
590 comparisons in PC1 were statistically significant: cocaine versus isoflurane controls (p = 0.011)
591 and cocaine versus K/X anesthesia (p = 0.001). Notably, K/X, saline-treated mice and isoflurane,
592 cocaine-treated mice segregate from one another in both PCA and UMAP space, indicating that
593 the K/X-induced changes are distinct from those induced by cocaine (**Figure 4D-F**). The similarity
594 in projection portraits for weights that contribute more to the K/X-treated group in $VTA^{DA}$→NAcLat
595 (**Figure 4U, V**) and all $VTA^{DA}$ neurons (**Figure 4W, X**) suggests that largely overlapping DA cells
596 may be targeted for each set of experiments and is consistent with the observation that
597 $VTA^{DA}$→NAcLat neurons comprise the majority of $VTA^{DA}$ neurons, as noted in previous studies[7,10].
598 These results thus serve as another proof of principle of the reliability of our approach to pull out
599 similar results from different datasets.
600
601 In addition to $VTA^{DA}$→NAcLat cells, we observed some segregation of isoflurane and K/X-treated
602 conditions in $VTA^{DA}$→Amygdala cells (**Figure 4G-I, R**). The lack of clear differentiation in PCA
603 space, with only PC3 showing significant differences between the isoflurane control group and
604 K/X anesthesia (One-way ANOVA p = 0.014, saline vs. K/X multiple comparisons adjusted p =
605 0.0078; **Figure S2**) makes it difficult to interpret which input sites may be contributing to the
606 differentiation in conditions that we observe. In the $VTA^{DA}$→NAcMed and $VTA^{DA}$→mPFC
607 subpopulations, the separation between isoflurane-saline, isoflurane-cocaine, and K/X-saline
608 conditions was much less pronounced (**Figure 4J-O, S-T**), and not to be significant; indeed,
609 similar separations were observed by chance (**Figure S3**). Notably, when considering inputs to
610 all $VTA^{DA}$ cells, the projection portraits that indicate the inputs most highly elevated or depressed
611 in K/X-treated mice highlight either the entire VTA, or the ventrolateral aspect of the VTA (**Figure**
612 **4U, V**). These projections are consistent with the locations of the $VTA^{DA}$→Amygdala and
613 $VTA^{DA}$→NAcLat cells, respectively, within the VTA. In contrast, the portraits do not highlight the
614 medial or ventromedial aspects of the VTA, which is the location of $VTA^{DA}$→mPFC and
615 $VTA^{DA}$→NAcMed cells[32,56]. These results together indicate that K/X anesthesia impacts inputs
616 that preferentially target $VTA^{DA}$→NAcLat or $VTA^{DA}$→Amygdala cells.
617
618 **Exploring gene expression patterns that predict changes in RABV input labeling**
619 We next wanted to explore if drug-induced changes in input connectivity might be related to gene
620 expression profiles in cells located in the input sites. The AGEA data are from all cells in the input
621 regions and are not limited to those projecting to the VTA and show only baseline gene expression

622 patterns and not those following drug administration. Nonetheless, these analyses can be a
623 valuable starting point in associating spatial gene expression data with patterns of RABV-labeled
624 inputs from $VTA^{DA}$ cells. To do this, we calculated the correlation of gene expression data from
625 the Allen Gene Expression Atlas (AGEA) with the difference (**Figure 5**) or the ratio (**Figure 6**)
626 between inputs labeled in each region in experimental conditions and isoflurane/saline-treated
627 controls. After filtering AGEA data for only high-quality experiments, we were left with 4,283 genes
628 to which we could calculate correlations within our 22 input brain regions of interest.
629
630 We first identified genes or pathways that may be linked to elevations or depressions in RABV
631 labeling for each condition. We selected genes that were highly positively or negatively correlated
632 to differences between 1) isoflurane-saline controls and 2) isoflurane- psychostimulant, morphine,
633 nicotine, or fluoxetine, or 3) K/X-saline mice. We used the top 50 genes in the AGEA that were
634 either positively or negatively correlated (Spearman's ρ) to differences in RABV labelling and
635 performed gene ontology (GO) analyses. Starting with drugs of abuse in aggregate, the 50 most
636 positively correlated genes (Spearman's $\rho > 0.47$, $p < 0.05$) were most significantly associated
637 with inhibitory ligand-gated chloride channels (**Figure 5A**), suggesting that higher basal
638 expression of these genes may be related to larger changes in connectivity induced by drugs of
639 abuse. Conversely, there were many more genes that were strongly negatively correlated to drug-
640 induced changes in RABV labeling. The 50 most negatively correlated genes (Spearman's $\rho < -$
641 $0.68$, $p < 0.001$) were most closely associated with negative regulation of long-term synaptic
642 potentiation (**Figure 5B**), suggesting that regulation of synaptic plasticity in input cell populations
643 may be a key indicator of the likelihood of a drug of abuse altering RABV input labeling. We
644 repeated this analysis of the top 50 genes with each individual drug: cocaine, methamphetamine,
645 amphetamine, morphine, and nicotine. In addition to findings in aggregate, other interesting
646 classes of genes that were negatively associated (Spearman's $\rho < -0.50$, $p < 0.05$) with individual
647 drug-induced changes in RABV labeling include regulation of synapse structural plasticity
648 (methamphetamine), regulation of calcium ion transport (nicotine), cellular response to $Ca^{2+}$ ions
649 (cocaine), and regulation of potassium ion transporters (nicotine) (**Figure S4**), which relate to
650 synaptic and cellular processes of plasticity and intrinsic excitability. There were fewer than 50
651 genes that were significantly positively correlated, but the top 50 genes (Spearman's $\rho > 0.36$, $p$
652 $< 0.12$) were associated with terms including anion channels (cocaine, amphetamine,
653 methamphetamine) and syntaxin binding (cocaine, amphetamine, nicotine) (**Figure S5**). We also
654 explored which gene expression patterns may be related to input changes driven by K/X
655 anesthesia. Anion channel activity, particularly GABA receptor expression, again shows up as

656 one of the most significant associations to the top 50 most positively correlated genes
657 (Spearman's $\rho > 0.37$, $p < 0.10$) (**Figure 5C**), while negatively correlated genes were associated
658 with a variety of metabolic processes (**Figure 5D**). Notably, these gene expression patterns were
659 not correlated with input changes induced by fluoxetine (**Figure S6**).
660
661 To further assess which classes of genes were the most closely related to the differences in drug
662 evoked RABV labeling relative to controls, we performed linear regressions of the ratios of RABV
663 labeling in experimental vs. control conditions relative to the mean of the log normalized
664 expression of AGEA RNA *in situ* hybridization data for a particular class of genes. We observed
665 an overall significant and slightly negative correlation between the RABV labeling ratio and the
666 gene expression mean ($r = -0.30$, $p = 2.1 \times 10^{-3}$) for all 4,283 genes (**Figure S7A**). This genome-
667 wide negative correlation is a useful reference to compare to correlation coefficients of subsets of
668 genes. Among the gene expression classes that we examined, the most significant association
669 was between the change in RABV-labeled inputs and ion channel gene expression ($r = -0.56$, $p$
670 $= 1.3 \times 10^{-9}$; **Figure 6A**), consistent with our results from GO analyses. The next most significant
671 classes were neurotransmitter receptors ($r = -0.46$, $p = 1.9 \times 10^{-6}$) and synapses ($r = -0.42$, $p =$
672 $1.6 \times 10^{-5}$), followed by genes that have been linked to SUDs through Genome-Wide Association
673 Studies (GWAS; $r = -0.33$, $p = 7.7 \times 10^{-4}$) as well as endo/exocytosis genes ($r = -0.30$, $p = 2.3 \times$
674 $10^{-3}$). Each of the above relationships showed a negative correlation of RABV ratios with gene
675 expression (**Figure 6B-C, S7B-C**). Except for endo/exocytosis genes, each class had a more
676 negative, significant correlation than our genome-wide reference. As a further comparison, we
677 observed that the relationships between RABV labeling ratios and gene classes that are likely
678 irrelevant to RABV labeling, such as mitochondrial genes ($r = -0.24$, $p = 1.4 \times 10^{-2}$), sugar
679 transporters ($r = -0.26$, $p = 1.0 \times 10^{-2}$), and tumor-associated genes ($r = -0.18$, $p = 7.0 \times 10^{-2}$) were
680 weaker and less significant than our classes of interest (**Figure S7D-F**).
681
682 As the class of ion channel genes was the most strongly correlated to drug-induced differences
683 in RABV-labeled input patterns, we assessed which ion channels are most closely linked to RABV
684 labeling differences between conditions. The most significant relationship was between $Ca^{2+}$
685 channel genes ($r = -0.57$, $p = 4.4 \times 10^{-10}$), followed by $Cl^-$ ($r = -0.39$, $p = 6.1 \times 10^{-5}$), $K^+$ ($r = -0.30$,
686 $p = 2.9 \times 10^{-3}$), and $Na^+$ channels ($r = -0.11$, $p = 0.30$; **Figure 6D-G**). The expression levels of
687 these channels, in particular $Ca^{2+}$ channels, are linked to regulating a variety of cellular processes,
688 including immediate early gene expression networks as well as cellular excitability. Ligand-gated
689 channels ($r = -0.40$, $p = 4.1 \times 10^{-5}$) were more strongly related with RABV labeling than voltage-

690 gated ion channels ($r = -0.33$, $p = 7.4 \times 10^{-4}$) or other types of ion channels ($r = -0.13$, $p = 0.21$;
691 **Figure S7G-I**). Among the ligand-gated channels, the glutamate receptors were the most strongly
692 correlated ($r = -0.49$, $p = 3.1 \times 10^{-7}$; **Figure 6H**). The next most strongly correlated gene classes
693 were acetylcholine receptors ($r = -0.36$, $p = 2.4 \times 10^{-4}$), GABA receptors ($r = -0.31$, $p = 1.8 \times 10^{-3}$),
694 and glycine receptors ($r = 0.32$, $p = 1.4 \times 10^{-3}$) (**Figure 6I-K**). Notably, glycine receptors were the
695 only class of genes that we analyzed that was positively correlated with RABV labeling. Similar
696 patterns were observed for K/X anesthetized mice (**Figure S8**), but not with isoflurane-
697 anesthetized, fluoxetine-treated mice (**Figure S9**). These results together indicate that the basal
698 expression levels of a variety of ion channels, particularly $Ca^{2+}$ and ligand-gated ion channels,
699 may be related to driving elevations or depressions in RABV labeling following a single injection
700 of a variety of drugs of abuse, or K/X anesthesia.
701
702 As the correlation between RABV labeling ratios and $Ca^{2+}$ channel gene expression is negative,
703 lower expression of $Ca^{2+}$ genes is linked to an elevation in drug-induced RABV input labeling. This
704 relationship could be explained by several mechanisms. One, expression of $Ca^{2+}$ channel genes
705 could be inhibitory towards the drug-induced change in RABV transmission. Alternatively, lower
706 $Ca^{2+}$ channel gene expression levels could indicate more potential for a drug-induced rise in gene
707 expression level. To differentiate between these possibilities, we performed CRISPR-based gene
708 expression modulation of the voltage-gated calcium ion channel *Cacna1e* using CRISPRi, which
709 reduces gene expression through blocking DNA transcription without cutting DNA[57] (**Figure 7A-**
710 **B**). Three different adeno-associated viruses (AAV) were co-injected into the NAcLat, an input
711 site to the VTA, in DAT-Cre mice. These viruses expressed 1) Cre, 2) Cre-dependent dCas9, 3)
712 Cre-dependent small guide RNA (gRNA) targeting *Cacna1e*. A two AAV mixture lacking the AAV
713 expressing the gRNA was used as a control. The three AAV experimental mix was administered
714 into the NAcLat in one hemisphere, while the two AAV control mix was injected into the other
715 hemisphere. During the same surgery, AAVs expressing Cre-dependent TVA-mCherry and rabies
716 virus glycoprotein were bilaterally injected into the VTA, so that RABV mapping could be done in
717 both hemispheres (**Figure 7C-D**). Because the NAcLat, NAcCore, and GPe unilaterally project to
718 the VTA in the same hemisphere, and not the contralateral VTA[7,10,15,25], the ratio of labeled inputs
719 in these sites on a single hemisphere can be used to assess the relative labeling in the NAcLat
720 in experimental and control conditions within each mouse.
721
722 We first validated that our CRISPRi strategy reduced *Cacna1e* gene expression. We designed
723 our gRNA to cause only a mild reduction in *Cacna1e* expression to more naturally mimic potential

724 changes in gene expression. We found that our CRISPRi perturbation reduced gene expression
725 by ~20% (**Figure 7E**). This knockdown of *Cacna1e* in the NAcLat via CRISPRi resulted in
726 decreased RABV-labeled inputs from the NAcLat compared to control mice where the shRNA
727 was not included (**Figure 7F**). These results indicate that reduced levels of *Cacna1e* lower the
728 number of RABV-labeled inputs from the NAcLat, suggesting that expression levels of *Cacna1e*
729 are directly related to RABV-labeled inputs. This means that expression of this gene is not
730 inhibitory towards RABV transmission. Therefore, a more likely hypothesis is that a low basal
731 gene expression of $Ca^{2+}$ channels allows for greater changes in the expression of these genes
732 following drug exposure.
733
734 **DISCUSSION:**
735 Here we explored the long-term consequences of a single injection of a variety of abused drugs
736 on the connectivity of $VTA^{DA}$ cells. We first confirmed that dimensionality reduction approaches
737 could adequately differentiate the connectivity between different cell populations in the VTA, and
738 showed which inputs differentiate DAergic, GABAergic, and glutamatergic cells in the VTA
739 (**Figure 1**). We then showed that a variety of drugs of abuse as well as K/X-based anesthesia
740 trigger long-lasting changes in the brain-wide input patterns to VTA cells, which were clearly
741 observable though less substantial than the differences onto different cell types or natural
742 variation in starter cell location (**Figures 2-3**). We used our cTRIO method to identify DA cell type-
743 specific changes induced by cocaine as well as K/X anesthesia, implicating the $VTA^{DA}$→NAcLat
744 and $VTA^{DA}$→Amygdala cells as those exhibiting the most substantial input changes (**Figure 4**).
745 We then explored intrinsic gene expression patterns throughout the brain that relate to the
746 elevation or depression in RABV labeling by different drugs, finding that expression levels of ion
747 channels, neurotransmitter receptors, and synapse-related genes were all significantly negatively
748 correlated with RABV input labeling ratios, with $Ca^{2+}$ channels and glutamate receptors being the
749 most strongly correlated (**Figure 6**). We then demonstrated the causative role of one calcium
750 channel gene, *Cacna1e*, in influencing RABV input mapping efficiency (**Figure 7**).
751
752 **Drugs of abuse induce changes in connectivity onto $VTA^{DA}$ neurons from common and**
753 **distributed input populations throughout the brain**
754 Using dimensionality reduction approaches we differentiated the input patterns to different VTA
755 cells (**Figure 1**) and showed that these differences were larger than the differences in inputs from
756 the same cell populations in animals given a drug of abuse vs. saline (**Figure 3A**). Notably, these
757 differences were unique from those triggered by the psychoactive but non-addictive substances

758 fluoxetine and K/X (**Figure 3C, F**). Differences were apparent on the 2nd PC axis, which were
759 driven by positive weights from the GPe, EP, EAM, LH, ZI, DR, and PBN, regions that showed
760 elevated connectivity in drug-treated mice. Many of these regions have been implicated in cocaine
761 addiction[58–61]. While these drug-induced differences in input labeling were less substantial than
762 intrinsic cell type connectivity differences (**Figure 3A**) or differences in starter cell location (**Figure**
763 **2N-S**), these differences are more apparent when using dimensionality reduction methods such
764 as PCA and UMAP. That different cell types exhibit larger differences in input patterns than the
765 same cell type with and without drug administration is perhaps not surprising, as different
766 populations of cells may receive different sets of inputs from one another, and these are likely
767 more stable across experiments than the differences in connectivity triggered following a single
768 exposure to a drug of abuse. The same is likely true for spatial gradients, which we determined
769 to be a major source of variation in RABV inputs to the VTA[32]. Notably, the minor differences in
770 starter cell location are likely not a technical concern specific to our study, but rather inherent to
771 all RABV mapping experiments that rely on intracranial injections, as a small amount of biological
772 or technical variation is to be expected. The PCA approach we employ here, however, can better
773 isolate these effects than traditional bar graph approaches and thus enable clearer observation
774 of the effect of the relevant variable being tested, here effects of a single drug administration (or
775 K/X anesthesia) on the input connectivity to $VTA^{DA}$ cells.
776
777 The results in this study further confirm our previous observations that a single exposure to a
778 variety of drugs of abuse triggers long-lasting changes in inputs to $VTA^{DA}$ neurons. Our
779 interpretation of these data is that the changes are largely being driven by a change in the activity
780 of input cells, as we have shown using fiber photometry and slice electrophysiology in three
781 separate studies[15,16,62]. However, we have not confirmed this to be true for all cases. As a single
782 exposure to a variety of drugs of abuse alters the strength of both excitatory and inhibitory inputs
783 in the VTA[5,20–22], we cannot rule out that changes in synapse number or strength may also
784 influence the observed connectivity results.
785
786 **Ketamine/xylazine anesthesia alters the input landscape of $VTA^{DA}$ cells**
787 Animals anesthetized with a K/X mixture showed a different pattern of input labeling to $VTA^{DA}$
788 cells than animals anesthetized with isoflurane (**Figure 4A-B**). While we cannot perform RABV
789 mapping on unanesthetized mice, making it impossible to definitively define which mode of
790 anesthesia, or both, alters RABV input patterns we suspect that isoflurane anesthesia has minimal
791 effect on the brain-wide inputs to $VTA^{DA}$ cells. This is largely because animals treated with a drug

792 of abuse with isoflurane anesthesia look more like those receiving K/X-saline than isoflurane-
793 saline animals (**Figure 3**). In addition, ketamine is a drug with known abuse potential[63–66]. While
794 the anesthetic doses used here (100 mg/kg) are well above the doses used recreationally (~1
795 mg/kg), the changes that we observed with K/X anesthesia may be related to the abuse potential
796 of ketamine. Interestingly, the K/X-induced input changes were most similar to those induced by
797 10 mg/kg of morphine (**Figure 3P-Q**). Antidepressant doses of ketamine may work in part via the
798 opioid system; indeed, it has been known for some time that ketamine binds the mu opioid
799 receptor[67–70], and it was more recently shown that the opioid antagonist naltrexone blocks the
800 antidepressant effects of ketamine[71,72]. Given that anesthetic doses of ketamine (100 mg/kg) are
801 roughly 10 times higher than antidepressant doses of ketamine (~10 mg/kg), K/X anesthesia
802 almost certainly engages the opioid system.
803
804 **Relationship of gene expression with the extent of drug-induced RABV input labeling**
805 Gene expression patterns in the mouse brain are correlated with the extent of elevations and
806 depressions of RABV labeling induced by one of several drugs of abuse. We observed a slightly
807 negative correlation of RABV labeling changes with the overall level of gene expression across
808 the brain. We are not sure of the implications of this negative correlation, though it could suggest
809 that if initial gene expression levels are lower, it leaves a higher potential for experience-induced
810 elevations. We observed significant negative correlations of RABV labeling changes induced by
811 drugs of abuse with the levels of expression of ion channel genes, neurotransmitter receptor-
812 related genes, and synapse-related genes. These results and our experiments demonstrating the
813 functional impact of downregulating *Cacna1e* for RABV input labeling (**Figure 7**) indicate that the
814 expression levels of these genes could be used as predictive biomarkers of which regions are
815 likely to undergo drug-induced changes in connectivity to $VTA^{DA}$ cells. They also suggest that the
816 expression levels of these gene classes are related to the drug-induced changes in RABV labeling.
817
818 While the AGEA is a useful resource for relating spatial gene expression information to our RABV
819 mapping datasets, there are notable limitations. First, the AGEA dataset is not as quantitatively
820 rigorous as modern single nucleus RNA sequencing or spatial transcriptomic datasets.
821 Nonetheless, we believe that the overall patterns of high and low expression, especially when
822 considered among classes of genes as was performed here, can still be informative. Furthermore,
823 the AGEA dataset provides a static picture of gene expression levels throughout the brain, and
824 thus does not account for potential changes in gene expression levels triggered by administration
825 of one of the drugs used in this study. Third, the AGEA dataset considers expression levels in all

826 cell types in a brain region, irrespective of their individual transcriptomic/molecular identities, while
827 only a subset of cells in a region project to $VTA^{DA}$ cells. Nonetheless, our CRISPRi experiment
828 showing that a mild reduction of *Cacna1e* reduces RABV labeling indicates the potential for
829 causative associations between gene expression patterns and drug-induced RABV input labeling
830 changes (**Figure 7**). This result also directly links cellular excitability and the extent to which RABV
831 labels these cells as monosynaptic inputs to defined cell populations.
832
833 Our RABV screen identified several input sites that show elevated or depressed labeling following
834 a single administration of a drug of abuse, suggesting potential changes in excitability of these
835 cells. $Ca^{2+}$ channel genes were also highly negatively correlated with the extent of drug-induced
836 changes in RABV input labeling. $Ca^{2+}$ channels have been implicated in substance abuse through
837 Genome-Wide Association Studies[73], and molecules that target these channels have shown some
838 promise as addiction therapeutics[74–79]. It is of particular interest that $Ca^{2+}$ and not $Cl^-$, $Na^+$, or $K^+$
839 channels are highly correlated to RABV input labeling changes. $Ca^{2+}$ is critically involved as a
840 secondary messenger in neurons that affects a variety of processes including long-lasting
841 changes in transcription and synaptic transmission, whereas the other ions are mostly involved
842 only in facilitating or inhibiting formation and propagation of the action potential. Understanding
843 how $Ca^{2+}$ channel gene expression levels relate to drug-induced changes in the brain will help to
844 illuminate the relationship between basal gene expression levels, drug-induced changes in RABV
845 labeling, and substance abuse, providing mechanistic insights into how inter-individual
846 differences influence susceptibility to substance abuse.
847
848 **ACKNOWLEDGEMENTS:**
849 We would like to thank Hemmings Wu and Zhoule Zhu for their thoughtful critique of our
850 manuscript.
851
852 **AUTHOR CONTRIBUTIONS:** KTB performed the viral tracing experiments, KB performed the
853 majority of computational analyses of the data, PD assisted with network constructions and
854 projection portraits, MH assisted with figure preparation, GT, JJV, and GA performed CRISPRi
855 experiments, and KB and KTB wrote the manuscript.
856
857 **FUNDING:** This work was supported by the NIH (R00 DA041445, DP2 AG067666, R01
858 DA054374, R01 DA056599, R01 NS130044), Tobacco Related Disease Research Program
859 (T31KT1437, T31P1426), American Parkinson Disease Association (APDA-5589562),

Alzheimer's Association (AARG-NTF-20-685694), New Vision Research (CCAD2020-002), Brightfocus Foundation (A2022031S), and the Brain and Behavior Research Foundation (NARSAD 26845) to KTB, NIH T32GM008620 and NIH F30DA056215 to MH, T32 GM136624 to KB and PD, and NSF GRFP DGE-1839285 to PD.

**COMPETING INTERESTS:** The authors have nothing to disclose.

**REFERENCES:**

1. Bromberg-Martin, E. S., Matsumoto, M. & Hikosaka, O. Dopamine in Motivational Control: Rewarding, Aversive, and Alerting. *Neuron* **68**, 815–834 (2010).
2. Lammel, S., Lim, B. K. & Malenka, R. C. Reward and aversion in a heterogeneous midbrain dopamine system. *Neuropharmacology* **76**, 351–359 (2014).
3. Wise, R. A. Dopamine, learning and motivation. *Nat Rev Neurosci* **5**, 483–494 (2004).
4. Kim, C. K. *et al.* Simultaneous fast measurement of circuit dynamics at multiple sites across the mammalian brain. *Nat Methods* **13**, 325–8 (2016).
5. Lammel, S., Ion, D. I., Roeper, J. & Malenka, R. C. Report Projection-Specific Modulation of Dopamine Neuron Synapses by Aversive and Rewarding Stimuli. *Neuron* **70**, 855–862 (2011).
6. Lammel, S. *et al.* Input-specific control of reward and aversion in the ventral tegmental area. *Nature* **491**, 212–217 (2012).
7. Beier, K. T. *et al.* Circuit Architecture of VTA Dopamine Neurons Revealed by Systematic Input-Output Mapping. *Cell* **162**, 622–634 (2015).
8. Menegas, W. *et al.* Dopamine neurons projecting to the posterior striatum form an anatomically distinct subclass. *Elife* **4**, 1–30 (2015).
9. Watabe-Uchida, M., Zhu, L., Ogawa, S. K., Vamanrao, A. & Uchida, N. Whole-Brain Mapping of Direct Inputs to Midbrain Dopamine Neurons. *Neuron* **74**, 858–873 (2012).
10. Beier, K. T. *et al.* Topological Organization of Ventral Tegmental Area Connectivity Revealed by Viral-Genetic Dissection of Input-Output Relations. *Cell Rep* **26**, 159-167.e6 (2019).
11. Cardozo Pinto, D. F. *et al.* Characterization of transgenic mouse models targeting neuromodulatory systems reveals organizational principles of the dorsal raphe. *Nat Commun* **10**, (2019).
12. Faget, L. *et al.* Afferent Inputs to Neurotransmitter-Defined Cell Types in the Ventral Tegmental Area. *Cell Rep* **15**, 2796–2808 (2016).
13. Kalivas, P. W. & Volkow, N. D. The neural basis of addiction: a pathology of motivation and choice. *Am J Psychiatry* **162**, 1403–1413 (2005).
14. Hyman, S. E., Malenka, R. C. & Nestler, E. J. Neural mechanisms of addiction: the role of reward-related learning and memory. *Annu Rev Neurosci* **29**, 565–598 (2006).
15. Beier, K. T. *et al.* Rabies screen reveals GPe control of cocaine-triggered plasticity. *Nature* **549**, 345–350 (2017).
16. Tian, G. *et al.* An extended Amygdal-midbrain circuit controlling cocaine withdrawal-induced anxiety and reinstatement. *Cell Rep* **39**, 1–16 (2022).

902 17. Juarez, B. & Han, M. H. Diversity of Dopaminergic Neural Circuits in Response to Drug
903 Exposure. *Neuropsychopharmacology* **41**, 2424–2446 (2016).
904 18. Mahler, S. V *et al.* Chemogenetic Manipulations of Ventral Tegmental Area Dopamine
905 Neurons Reveal Multifaceted Roles in Cocaine Abuse. *Journal of Neuroscience* **39**, 503–
906 518 (2019).
907 19. Saal, D., Dong, Y., Bonci, A. & Malenka, R. C. Drugs of abuse and stress trigger a
908 common synaptic adaptation in dopamine neurons. *Neuron* **37**, 577–582 (2003).
909 20. Ungless, M. A., Whistler, J. L., Malenka, R. C. & Bonci, A. Single cocaine exposure in
910 vivo induces long-term potentiation in dopamine neurons. *Nature* **411**, 583–7. (2001).
911 21. Niehaus, J. L., Murali, M. & Kauer, J. A. Drugs of abuse and stress impair LTP at
912 inhibitory synapses in the ventral tegmental area. *European Journal of Neuroscience* **32**,
913 108–117 (2010).
914 22. Bocklisch, C. *et al.* Cocaine Disinhibits Dopamine Neurons by Potentiation of GABA
915 Transmission in the Ventral Tegmental Area. *Science (1979)* **341**, 1521–1525 (2013).
916 23. Dong, Y. *et al.* Cocaine-induced potentiation of synaptic strength in dopamine neurons:
917 behavioral correlates in GluRA(-/-) mice. *Proc Natl Acad Sci U S A* **101**, 14282–14287
918 (2004).
919 24. Creed, M. *et al.* Cocaine exposure enhances the activity of ventral tegmental area
920 dopamine neurons via calcium-impermeable NMDARs. *Journal of Neuroscience* **36**,
921 10759–10768 (2016).
922 25. Tian, G. *et al.* An extended Amygdala-midbrain circuit controlling cocaine withdrawal-
923 induced anxiety and reinstatement. *Cell Rep* **39**, 1–16 (2022).
924 26. Backman, C. M. *et al.* Characterization of a mouse strain expressing Cre recombinase
925 from the 3' untranslated region of the dopamine transporter locus. *Genesis* **44**, 383–390
926 (2006).
927 27. Taniguchi, H. *et al.* A Resource of Cre Driver Lines for Genetic Targeting of GABAergic
928 Neurons in Cerebral Cortex. *Neuron* **71**, 995–1013 (2011).
929 28. Vong, L. *et al.* Leptin Action on GABAergic Neurons Prevents Obesity and Reduces
930 Inhibitory Tone to POMC Neurons. *Neuron* **71**, 142–154 (2011).
931 29. Kumar, N. *et al.* The development of an AAV-based crispr sacas9 genome editing system
932 that can be delivered to neurons in vivo and regulated via doxycycline and cre-
933 recombinase. *Front Mol Neurosci* **11**, 1–14 (2018).
934 30. Pedregosa, F. *et al.* Scikit-learn: Machine Learning in Python. *Journal of Machine*
935 *Learning Research* **12**, 2825–2830 (2011).
936 31. McInnes, L., Healy, J. & Melville, J. UMAP: Uniform Manifold Approximation and
937 Projection for Dimension Reduction. *ArXiv* **1802.03426**, 1–51 (2018).
938 32. Derdeyn, P., Hui, M., Macchia, D. & Beier, K. Uncovering the Connectivity Logic of the
939 Ventral Tegmental Area. *Front Neural Circuits* **15**, 799688 (2022).
940 33. Waskom, M. Seaborn: Statistical Data Visualization. *J Open Source Softw* **6**, 3021
941 (2021).
942 34. Hunter, J. D. Matplotlib: a 2D graphics environment. *Comput Sci Eng* **9**, 90–95 (2007).
943 35. Oh, S. W. *et al.* A mesoscale connectome of the mouse brain. *Nature* **508**, 207–214
944 (2014).

945 36. Lein, E. S. *et al.* Genome-wide atlas of gene expression in the adult mouse brain. *Nature*
946 **445**, 168–176 (2007).
947 37. Brynildsen, J. K. *et al.* Gene coexpression patterns predict opiate-induced brain-state
948 transitions. *Proc Natl Acad Sci U S A* **117**, 19556–19565 (2020).
949 38. Fulcher, B. D., Murray, J. D., Zerbi, V. & Wang, X. J. Multimodal gradients across mouse
950 cortex. *Proc Natl Acad Sci U S A* **116**, 4689–4695 (2019).
951 39. Sian, J., Youdim, M. & Riederer, P, et al. Biochemical Anatomy of the Basal Ganglia and
952 Associated Neural Systems. in *Basic Neurochemistry: Molecular, Cellular and Medical*
953 *Aspects.* (eds. Siegel, G., Agranoff, B. & Albers, RW, et al.) (1999).
954 40. Xie, Z. *et al.* Gene Set Knowledge Discovery with Enrichr. *Curr Protoc* **1**, 1–51 (2021).
955 41. Ji, X., Zhang, H. & Cui, Q. A Panel of Synapse-Related Genes as a Biomarker for
956 Gliomas. *Front Neurosci* **14**, 1–8 (2020).
957 42. Wang, R. *et al.* Ion channel gene expression predicts survival in glioma patients. *Sci Rep*
958 **5**, 1–10 (2015).
959 43. Berchtold, N. C. *et al.* Synaptic genes are extensively downregulated across multiple
960 brain regions in normal human aging and Alzheimer's disease. *Neurobiol Aging* **34**,
961 1653–1661 (2013).
962 44. Shi, L. *et al.* AddictGene: An integrated knowledge base for differentially expressed
963 genes associated with addictive substance. *Comput Struct Biotechnol J* **19**, 2416–2422
964 (2021).
965 45. Saheki, Y. & De Camilli, P. Synaptic vesicle endocytosis. *Cold Spring Harb Perspect Biol*
966 **4**, (2012).
967 46. Harding, S. D. *et al.* The IUPHAR/BPS guide to PHARMACOLOGY in 2022: Curating
968 pharmacology for COVID-19, malaria and antibacterials. *Nucleic Acids Res* **50**, D1282–
969 D1294 (2022).
970 47. Yamaguchi, T., Wang, H. L., Li, X., Ng, T. H. & Morales, M. Mesocorticolimbic
971 glutamatergic pathway. *Journal of Neuroscience* **31**, 8476–8490 (2011).
972 48. Yamaguchi, T., Sheen, W. & Morales, M. Glutamatergic neurons are present in the rat
973 ventral tegmental area. *European Journal of Neuroscience* **25**, 106–118 (2007).
974 49. Root, D. H. *et al.* Single rodent mesohabenular axons release glutamate and GABA. *Nat*
975 *Neurosci* **17**, 1543–1551 (2014).
976 50. Morales, M. & Margolis, E. B. Ventral tegmental area: Cellular heterogeneity, connectivity
977 and behaviour. *Nat Rev Neurosci* **18**, 73–85 (2017).
978 51. Hnasko, T. S., Hjelmstad, G. O., Fields, H. L. & Edwards, R. H. Ventral tegmental area
979 glutamate neurons: electrophysiological properties and projections. *Journal of*
980 *Neuroscience* **32**, 15076–15085 (2012).
981 52. Kim, J. I. *et al.* Aldehyde dehydrogenase 1a1 mediates a GABA synthesis pathway in
982 midbrain dopaminergic neurons. *Science (1979)* **350**, 102–106 (2015).
983 53. Tritsch, N. X., Ding, J. B. & Sabatini, B. L. Dopaminergic neurons inhibit striatal output
984 through non-canonical release of GABA. *Nature* **490**, 262–266 (2012).
985 54. Koob, G. F. A Role for Brain Stress Systems in Addiction. *Neuron* **59**, 11–34 (2008).
986 55. Koob, G. F. Brain stress systems in the amygdala and addiction. *Brain Res* **1293**, 61–75
987 (2009).

988 56. Lammel, S. *et al.* Unique Properties of Mesoprefrontal Neurons within a Dual
989 Mesocorticolimbic Dopamine System. *Neuron* **57**, 760–773 (2008).
990 57. Larson, M. H. *et al.* CRISPR interference (CRISPRi) for sequence-specific control of gene
991 expression. *Nat Protoc* **8**, 2180–2196 (2013).
992 58. Li, H. *et al.* Entopeduncular nucleus projections to the lateral habenula contribute to
993 cocaine avoidance. *Journal of Neuroscience* **41**, 298–306 (2021).
994 59. López, A. J. *et al.* Medial habenula cholinergic signaling regulates cocaine-associated
995 relapse-like behavior. *Addiction Biology* **24**, 403–413 (2019).
996 60. Tan, D., Nuno-Perez, A., Mameli, M. & Meye, F. J. Cocaine withdrawal reduces GABABR
997 transmission at entopeduncular nucleus – lateral habenula synapses. *European Journal
998 of Neuroscience* **50**, 2124–2133 (2019).
999 61. Koob, G. F. & Volkow, N. D. Neurocircuitry of addiction. *Neuropsychopharmacology* **35**,
1000 217–238 (2010).
1001 62. Tian, G. *et al.* Molecular and circuit determinants in the globus pallidus mediating control
1002 of cocaine-induced behavioral plasticity. *Neuron Sneak Peek* (2023).
1003 63. Liu, Y., Lin, D., Wu, B. & Zhou, W. Ketamine abuse potential and use disorder. *Brain Res
1004 Bull* **126**, 68–73 (2016).
1005 64. Ni, A., Lee Cantrell, F. & Clark, R. F. Ketamine exposure demographics and outcomes
1006 over 16 years as reported to US poison centers. *American Journal of Emergency
1007 Medicine* **36**, 1459–1462 (2018).
1008 65. Dillon, P., Copeland, J. & Jansen, K. Patterns of use and harms associated with non-
1009 medical ketamine use. *Drug Alcohol Depend* **69**, 23–28 (2003).
1010 66. Morgan, C. J. A. & Curran, H. V. Ketamine use: A review. *Addiction* **107**, 27–38 (2012).
1011 67. Ryder, S., Way, W. L. & Trevor, A. J. Comparative pharmacology of the optical isomers of
1012 ketamine in mice. *Eur J Pharmacol* **49**, 15–23 (1978).
1013 68. Finck, A. D. & Ngai, S. H. Opiate receptor mediation of ketamine analgesia. *Anesth Analg
1014* **56**, 291–297 (1982).
1015 69. Hustveit, O., Maurset, A. & Oye, I. Interaction of the Chiral Forms of Ketamine with
1016 Opioid, Phencyclidine, c and Muscarinic Receptors. *Pharmacol Toxicol* **77**, 355–359
1017 (1995).
1018 70. Bonaventura, J. *et al.* Pharmacological and behavioral divergence of ketamine
1019 enantiomers:implications for abuse liability. *Mol Psychiatry* **26**, 6704–6722 (2021).
1020 71. Williams, N. R. *et al.* Attenuation of antidepressant and antisuicidal effects of ketamine by
1021 opioid receptor antagonism. *Mol Psychiatry* **24**, 1779–1786 (2019).
1022 72. Williams, N. R. *et al.* Attenuation of antidepressant effects of ketamine by opioid receptor
1023 antagonism. *American Journal of Psychiatry* **175**, 1205–1215 (2018).
1024 73. Gelernter, J. *et al.* Genome-wide association study of opioid dependence: Multiple
1025 associations mapped to calcium and potassium pathways. *Biol Psychiatry* **76**, 66–74
1026 (2014).
1027 74. Malcolm, R., Brady, K. T., Moore, J. & Kajdasz, D. Amlodipine treatment of cocaine
1028 dependence. *J Psychoactive Drugs* **31**, 117–120 (1999).
1029 75. Altamura, A. C., Regazzetti, M. G. & Porta, M. Nimodipine in human alcohol withdrawal
1030 syndrome - an open study. *European Neuropsychopharmacology* **1**, 37–40 (1990).

1031 76. Rosse, R. *et al.* Nimodipine Pharmacotherapeutic Adjuvant Therapy for Inpatient
1032 Treatment of Cocaine Dependence. *Clin Neuropharmacol* **17**, 348–358 (1994).
1033 77. Muntaner, C., Kumor, K., Nagoshi, C. & Jaffe, J. Effect of nifedipine pretreatment on
1034 subjective and cardiovascular responses to intravenous cocaine in humans. *Drug Alcohol*
1035 *Depend* **105**, 37–41 (1991).
1036 78. Johnson, B. A. *et al.* Effects of Isradipine on Cocaine-Induced Subjective Mood. *J Clin*
1037 *Psychopharmacol* **24**, 180–191 (2004).
1038 79. Vaupel, D. B., Lange, W. R. & London, E. D. Effects of verapamil on morphine-induced
1039 euphoria, analgesia and respiratory depression in humans. *Journal of Pharmacology and*
1040 *Experimental Therapeutics* **267**, 1386–1394 (1993).
1041
1042

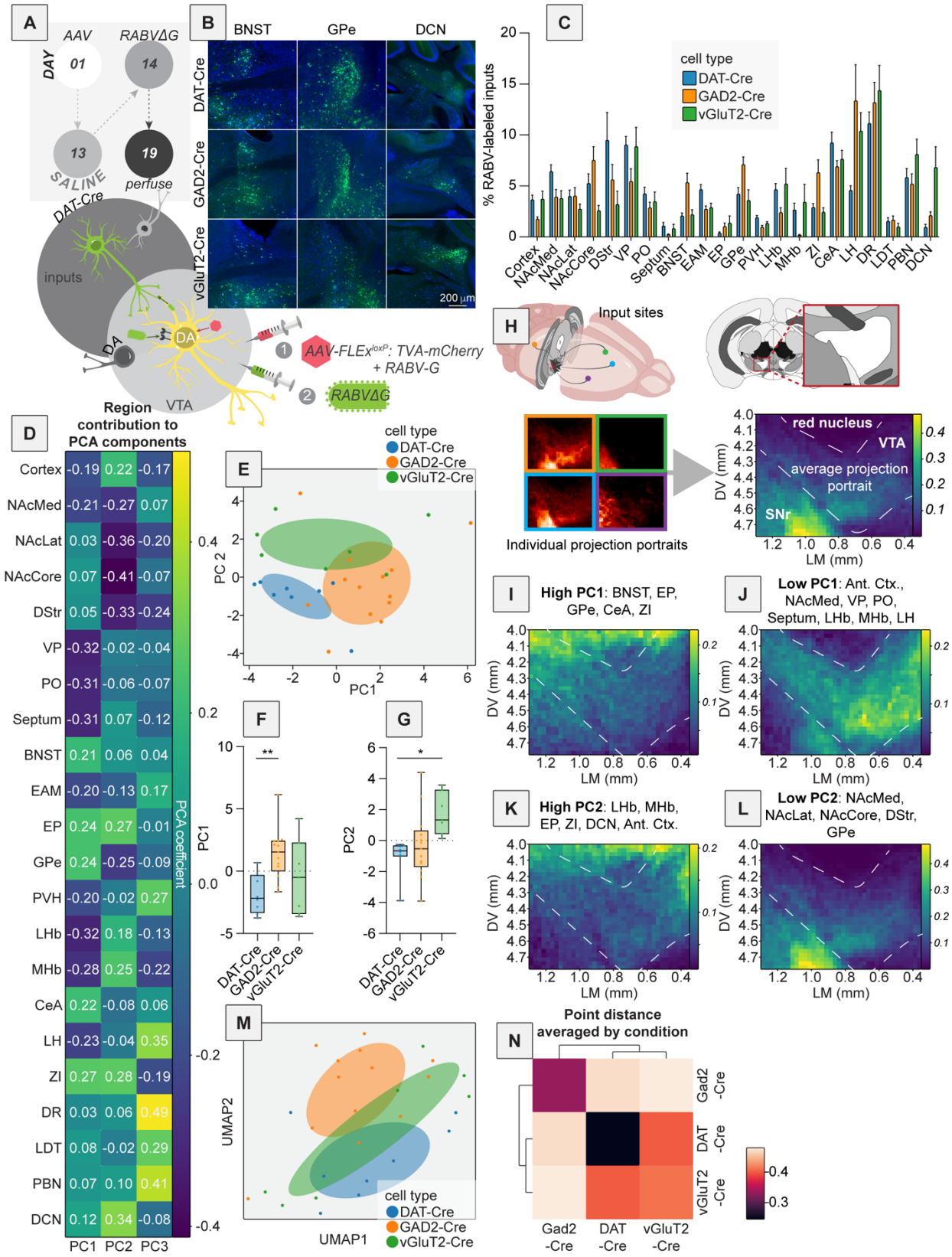
A
AAV
RABVΔG
DAY
01
14
13
19
SALINE
perfuse
DAT-Cre
inputs
DA
VTA
AAV-FLEx^loxP: TVA-mCherry + RABV-G
RABVΔG
B
BNST
GPe
DCN
DAT-Cre
GAD2-Cre
vGluT2-Cre
200 µm
C
% RABV-labeled inputs
cell type
DAT-Cre
GAD2-Cre
vGluT2-Cre
Cortex
NAcMed
NAcLat
NAcCore
DStr
VP
PO
Septum
BNST
EAM
EP
GPe
PVH
LHb
MHb
ZI
CeA
LH
DR
LDT
PBN
DCN
H
Input sites
Individual projection portraits
red nucleus
VTA
average projection portrait
SNr
DV (mm)
LM (mm)
D
Region contribution to PCA components
PCA coefficient
PC1
PC2
PC3
E
PC 2
PC1
F
PC1
G
PC2
M
UMAP2
UMAP1
I
High PC1: BNST, EP, GPe, CeA, ZI
J
Low PC1: Ant. Ctx., NAcMed, VP, PO, Septum, LHb, MHb, LH
K
High PC2: LHb, MHb, EP, ZI, DCN, Ant. Ctx.
L
Low PC2: NAcMed, NAcLat, NAcCore, DStr, GPe
N
Point distance averaged by condition
Gad2-Cre
DAT-Cre
vGluT2-Cre

1043

1044 **Figure 1: Dimensionality reduction of RABV input tracing to 3 different VTA cell types.**
1045 (A) Schematic and timeline of viral injections into mice.
1046 (B) Representative images of the BNST, GPe, and DCN of DAT-Cre, GAD2-Cre, and vGlut2-Cre
1047 mice. Green indicates RABV-labeled cells. Scale, 200 μm.
1048 (C) Bar plot showing percent of RABV-labeled cells in each input region for DAT-Cre, GAD2-Cre,
1049 and vGlut2-Cre mice.
1050 (D) Heatmap of the contributions of each brain region, or feature, in the data to PCs 1 through 3.
1051 (E) PCA of input labeling from brains from DAT-Cre, GAD2-Cre, and vGlut2-Cre mice. For this
1052 and other figures, ellipsoids were centered at the average coordinate of a condition and stretched
1053 one standard deviation along the primary and secondary axes.
1054 (F) Box plot comparisons of PC1. One-way ANOVA $p = 0.010$, pairwise t-tests DAT-Cre vs.
1055 GAD2-Cre multiple comparisons adjusted $p = 0.0087$, DAT-Cre vs. vGluT2-Cre $p = 0.46$, GAD2-
1056 Cre vs. vGluT2-Cre $p = 0.19$. n=8 for DAT-Cre, n = 13 for GAD2-Cre, and n = 7 for vGluT2-Cre.
1057 (G) Box plot comparisons of PC1. One-way ANOVA $p = 0.016$, pairwise t-tests DAT-Cre vs.
1058 GAD2-Cre multiple comparisons adjusted $p = 0.65$, DAT-Cre vs. vGluT2-Cre $p = 0.016$, GAD2-
1059 Cre vs. vGluT2-Cre $p = 0.051$.
1060 (H) Schematic of how projection portraits are constructed. A representative slice of the VTA is
1061 considered for experiments from the Allen Mouse Brain Connectivity Atlas with injections into
1062 relevant brain regions that provide input to the VTA. Projection density values in this slice are
1063 averaged and visualized to obtain the projection portrait in the VTA for that group of regions.
1064 (I) Projection portrait of the VTA based on inputs from regions with a high positive contribution to
1065 PC1: BNST, EP, GPe, CeA, and ZI.
1066 (J) Projection portrait of the VTA based on inputs from regions with a large negative contribution
1067 to PC1: anterior cortex, NAcMed, VP, PO, septum, LHb, MHb, and LH.
1068 (K) Projection portrait of the VTA based on inputs from regions with a high positive contribution to
1069 PC2: LHb, MHb, EP, ZI, DCN, and anterior cortex.
1070 (L) Projection portrait of the VTA based on inputs from regions with a large negative contribution
1071 to PC2: NAcMed, NAcLat, NAcCore, DStr, and GPe.
1072 (M) UMAP embedding of input labeling of brains from DAT-Cre, GAD2-Cre, and vGlut2-Cre mice.
1073 (N) Correlogram generated using the average Euclidean distance of data points from each other
1074 from 20 UMAP embeddings.
1075

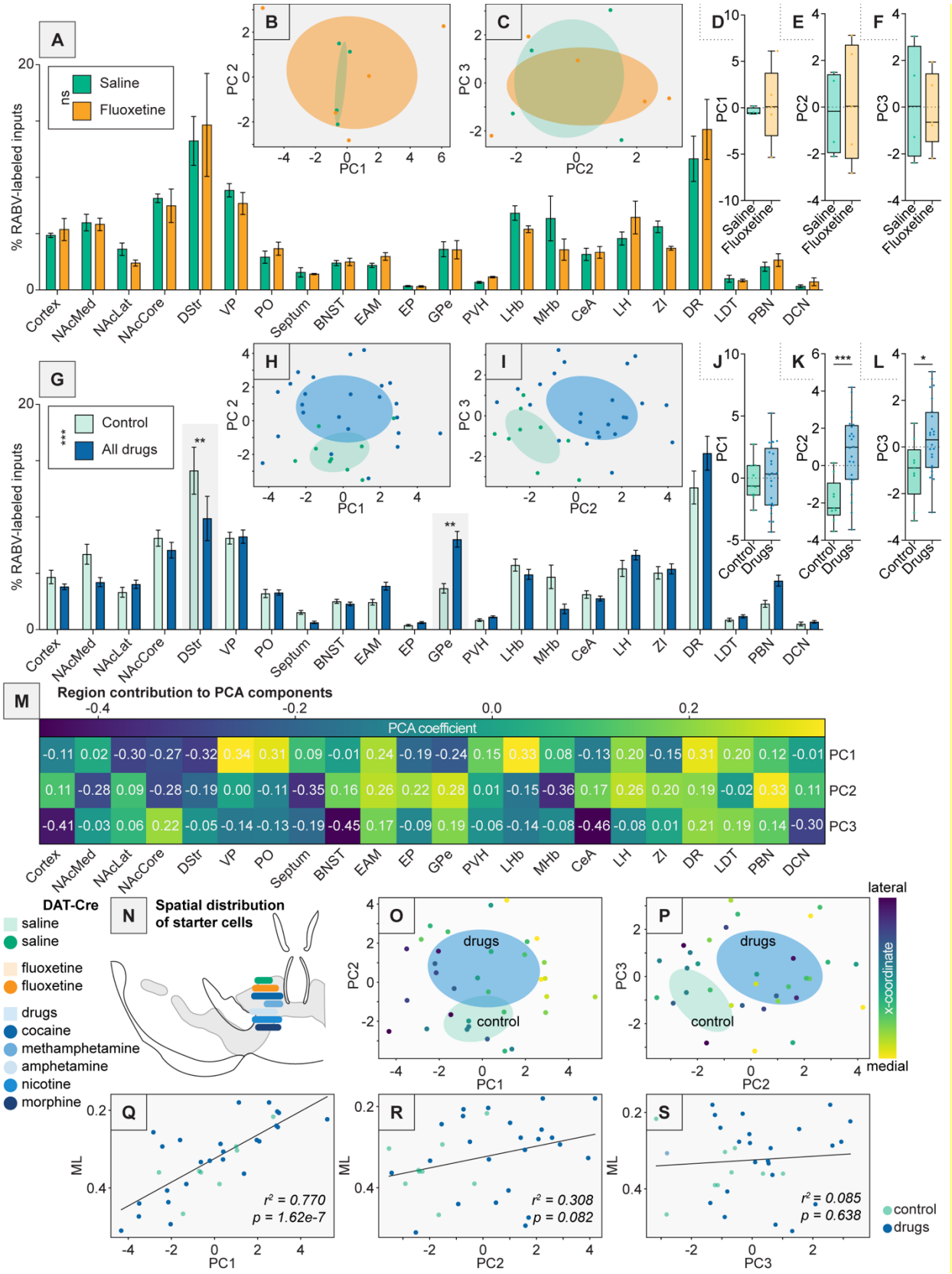
A
Saline
Fluoxetine
ns
% RABV-labeled inputs
B
C
D
E
F
PC 2
PC 3
PC1
PC2
PC3
Saline
Fluoxetine
Cortex
NAcMed
NAcLat
NAcCore
DStr
VP
PO
Septum
BNST
EAM
EP
GPe
PVH
LHb
MHb
CeA
LH
ZI
DR
LDT
PBN
DCN
G
Control
All drugs
***
**
H
I
J
K
L
Control
Drugs
M
Region contribution to PCA components
PCA coefficient
-0.11 0.02 -0.30 -0.27 -0.32 0.34 0.31 0.09 -0.01 0.24 -0.19 -0.24 0.15 0.33 0.08 -0.13 0.20 -0.15 0.31 0.20 0.12 -0.01 PC1
0.11 -0.28 0.09 -0.28 -0.19 0.00 -0.11 -0.35 0.16 0.26 0.22 0.28 0.01 -0.15 -0.36 0.17 0.26 0.20 0.19 -0.02 0.33 0.11 PC2
-0.41 -0.03 0.06 0.22 -0.05 -0.14 -0.13 -0.19 -0.45 0.17 -0.09 0.19 -0.06 -0.14 -0.08 -0.46 -0.08 0.01 0.21 0.19 0.14 -0.30 PC3
DAT-Cre
saline
saline
fluoxetine
fluoxetine
drugs
cocaine
methamphetamine
amphetamine
nicotine
morphine
N
Spatial distribution of starter cells
O
P
drugs
control
lateral
medial
x-coordinate
Q
R
S
ML
r² = 0.770
p = 1.62e-7
r² = 0.308
p = 0.082
r² = 0.085
p = 0.638
control
drugs

1076

1077

1078 **Figure 2: PCA can deconvolve drug-induced effects from experimental variation.**
1079 (A) Bar graph representation of inputs from DAT-Cre mice anesthetized with isoflurane and
1080 treated with a single injection of saline or fluoxetine. N = 4 for saline, n = 5 for fluoxetine. Two-
1081 way ANOVA, p = 0.91.
1082 (B) PCA plot showing PC1 and PC2 of brains from saline or fluoxetine-treated mice.
1083 (C) PCA plot showing PC2 and PC3 of brains from saline or fluoxetine-treated mice.
1084 (D) Box plot of PC1, p = 0.75. n = 4 for saline, n = 5 for fluoxetine.
1085 (E) Box plot of PC2, p = 0.78.
1086 (F) Box plot of PC3, p = 0.81.
1087 (G) Bar graph representation of inputs from DAT-Cre mice anesthetized with isoflurane and
1088 treated with a single injection of saline or fluoxetine (controls), or one of the drugs of abuse
1089 cocaine, methamphetamine, amphetamine, nicotine, or morphine. n = 9 for control, n = 24 for
1090 combined drugs of abuse. Two-way ANOVA, p = 0.0001; unpaired t-tests with Sidak corrections
1091 for multiple comparisons: DStr, p = 0.0051, GPe, p = 0.0036.
1092 (H) PCA plot showing PC1 and PC2 of brains from control or drug-treated mice.
1093 (I) PCA plot showing PC2 and PC3 of brains from control or drug-treated mice.
1094 (J) Box plot of PC1, p = 0.78. n = 9 for control, n = 24 for drugs.
1095 (K) Box plot of PC2, p = 0.0009.
1096 (L) Box plot of PC3, p = 0.024.
1097 (M) Heatmap of the contributions of each brain region to PC1 through PC3 for data shown in
1098 panels E-F.
1099 (N) Distribution of the starter cell center of mass along the medial-lateral axis for each
1100 experimental condition. Saline n = 4, fluoxetine n = 5, cocaine n = 5, methamphetamine n = 4,
1101 amphetamine n = 5, nicotine n = 5, morphine n = 5.
1102 (O) PC1 vs. PC2 for control vs. drug conditions as shown in E, with each point colored according
1103 to the medial-lateral coordinate of the center of mass of starter cells for each brain.
1104 (P) PC2 vs. PC3 for control vs. drug conditions as shown in F, with each point colored according
1105 to the medial-lateral coordinate of the center of mass of starter cells for each brain.
1106 (Q) Linear regression between the x-coordinate of the center of mass of starter cells for each
1107 brain vs. PC1. $r^2$ = 0.770, p = 1.62e-7,
1108 (R) Linear regression between the x-coordinate of the center of mass of starter cells for each brain
1109 vs. PC2. $r^2$ = 0.308, p = 0.082.
1110 (S) Linear regression between the x-coordinate of the center of mass of starter cells for each brain
1111 vs. PC3, $r^2$ = 0.085, p = 0.638.

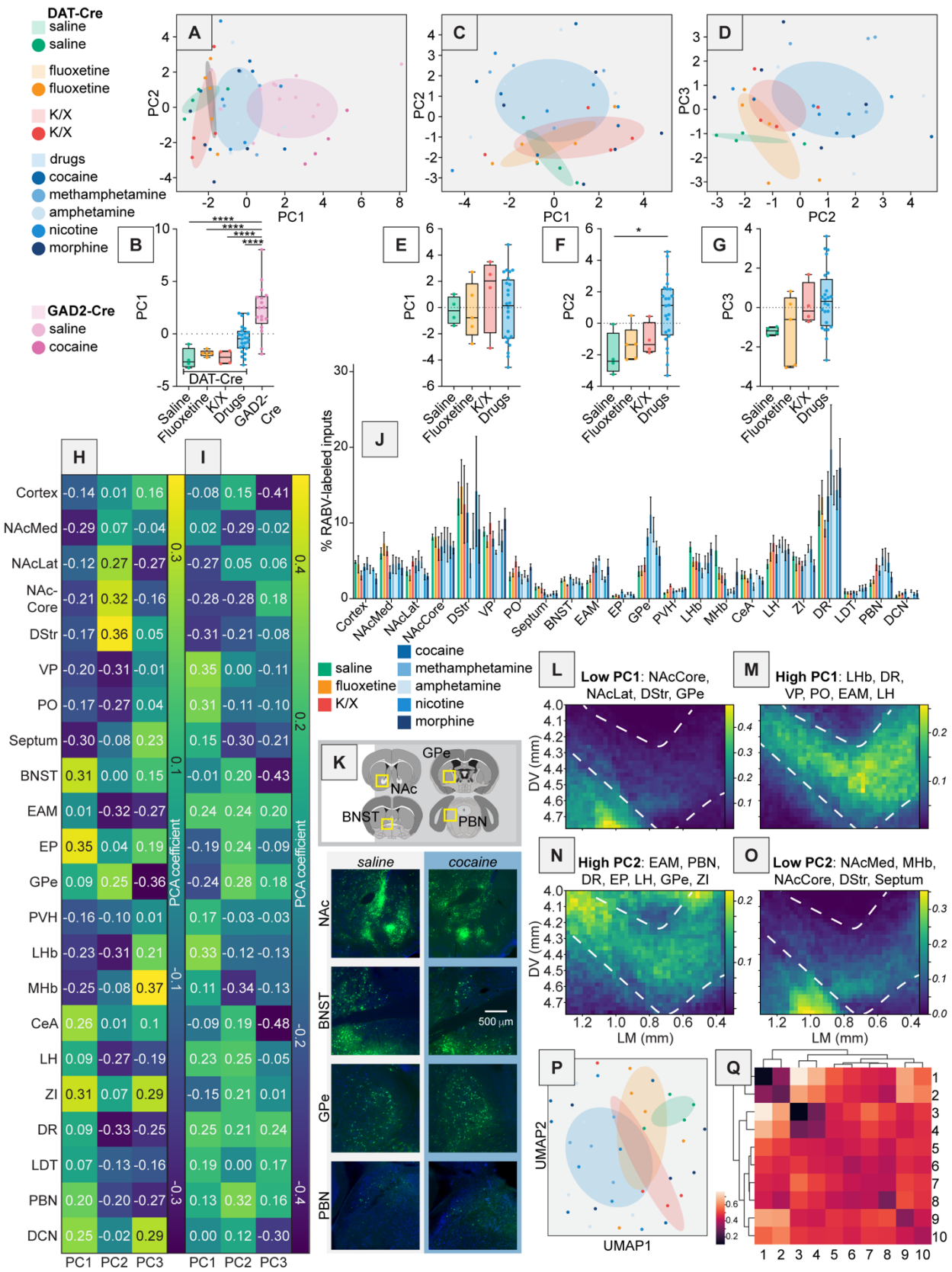
DAT-Cre
saline
saline
fluoxetine
fluoxetine
K/X
K/X
drugs
cocaine
methamphetamine
amphetamine
nicotine
morphine
GAD2-Cre
saline
cocaine
A
B
C
D
E
F
G
H
I
J
K
L
M
N
O
P
Q
PC1
PC2
PC3
DAT-Cre
Saline
Fluoxetine
K/X
Drugs
GAD2-Cre
% RABV-labeled inputs
Cortex
NAcMed
NAcLat
NAcCore
DStr
VP
PO
Septum
BNST
EAM
EP
GPe
PVH
LHb
MHb
CeA
LH
ZI
DR
LDT
PBN
DCN
PCA coefficient
saline
fluoxetine
K/X
cocaine
methamphetamine
amphetamine
nicotine
morphine
NAc
BNST
GPe
PBN
saline
cocaine
500 µm
Low PC1: NAcCore, NAcLat, DStr, GPe
High PC1: LHb, DR, VP, PO, EAM, LH
High PC2: EAM, PBN, DR, EP, LH, GPe, ZI
Low PC2: NAcMed, MHb, NAcCore, DStr, Septum
DV (mm)
LM (mm)
UMAP1
UMAP2

1112

1113 **Figure 3: Dimensionality reduction analysis of brains from animals treated with a single**
1114 **drug exposure.**
1115 (A) PCA plot showing PC1 and PC2 of brains from DAT-Cre and GAD2-Cre mice. DAT-Cre mice
1116 were anesthetized with K/X and treated with saline or anesthetized with isoflurane and treated
1117 with saline or one of the drugs cocaine, methamphetamine, amphetamine, nicotine, morphine, or
1118 fluoxetine. GAD2-Cre mice were anesthetized with isoflurane and treated with saline or cocaine.
1119 (B) Box plot of PC1, One-way ANOVA $p < 0.0001$, pairwise t-tests DAT-Cre saline vs. DAT-Cre
1120 fluoxetine multiple comparisons adjusted $p = 0.99$, DAT-Cre saline vs. DAT-Cre K/X $p = 1.0$, DAT-
1121 Cre saline vs. DAT-Cre drugs $p = 0.23$, DAT-Cre saline vs. GAD2-Cre $p < 0.0001$, DAT-Cre
1122 fluoxetine vs. DAT-Cre K/X $p = 1.0$, DAT-Cre fluoxetine vs. DAT-Cre drugs $p = 0.46$, DAT-Cre
1123 fluoxetine vs. GAD2-Cre $p < 0.0001$, DAT-Cre K/X vs. DAT-Cre drugs $p = 0.31$, DAT-Cre K/X vs.
1124 GAD2-Cre $p < 0.0001$, DAT-Cre drugs vs. GAD2-Cre $p < 0.0001$. $n = 4$ for DAT-Cre saline and
1125 DAT-Cre K/X, $n = 5$ for DAT-Cre fluoxetine, $n = 24$ for DAT-Cre drugs, $n = 17$ for GAD2-Cre.
1126 (C) PCA plot showing PC1 and PC2 of brains from DAT-Cre mice anesthetized with isoflurane
1127 and treated with cocaine, methamphetamine, amphetamine, nicotine, morphine, fluoxetine, or
1128 saline, or anesthetized with K/X and treated with saline.
1129 (D) PC2 and PC3 of the same group of brains as shown in panel B.
1130 (E) Box plot of PC1, One-way ANOVA $p = 0.81$.
1131 (F) Box plot of PC2, One-way ANOVA $p = 0.0093$, pairwise t-tests DAT-Cre saline vs. DAT-Cre
1132 fluoxetine multiple comparisons adjusted $p = 0.94$, DAT-Cre saline vs. DAT-Cre K/X $p = 0.87$,
1133 DAT-Cre saline vs. DAT-Cre drugs $p = 0.034$, DAT-Cre fluoxetine vs. DAT-Cre K/X $p = 0.99$, DAT-
1134 Cre fluoxetine vs. DAT-Cre drugs $p = 0.10$, DAT-Cre K/X vs. DAT-Cre drugs $p = 0.27$.
1135 (G) Box plot of PC3, One-way ANOVA $p = 0.086$.
1136 (H) Heatmap of the contributions of each brain region to PC1 through PC3 for data shown in panel
1137 A.
1138 (I) Heatmap of the contributions of each brain region to PC1 through PC3 for data shown in panels
1139 B and C.
1140 (J) Bar plot showing percent of RABV-labeled cells in each input region for the DAT-Cre mice
1141 shown in panel B.
1142 (K) Representative images of brain slices from DAT-Cre mice showing, from top to bottom, the
1143 NAc, BNST, GPe, and PBN. Scale, 500 $\mu$m.
1144 (L) Projection portrait of the VTA based on inputs from regions with a large negative contribution
1145 to PC1, based on data from panel E: NAcCore, NAcLat, DStr, GPe.

1146 (M) Projection portrait based on inputs from regions with a high positive contribution to PC1, based
1147 on data from panel E: LHb, DR, VP, PO, EAM, LH.
1148 (N) Projection portrait based on inputs from regions with a high positive contribution to PC2, based
1149 on data from panel E: EAM, PBN, DR, EP, LH, GPe, ZI.
1150 (O) Projection portrait based on inputs from regions with a large negative contribution to PC2,
1151 based on data from panel E: NAcMed, NAcCore, DStr, Septum, MHb.
1152 (P) UMAP embedding of data from the brains of DAT-Cre mice shown in panels B and F.
1153 (Q) Correlogram showing average Euclidean distance of data points over 20 UMAP embeddings
1154 of the data presented in panel J. Experiment conditions from bottom to top and left to right are
1155 labelled 1-10 and are ordered as follows: GAD2-Cre cocaine, GAD2-Cre saline, saline, fluoxetine,
1156 cocaine, nicotine, amphetamine, meth, K/X, and morphine.

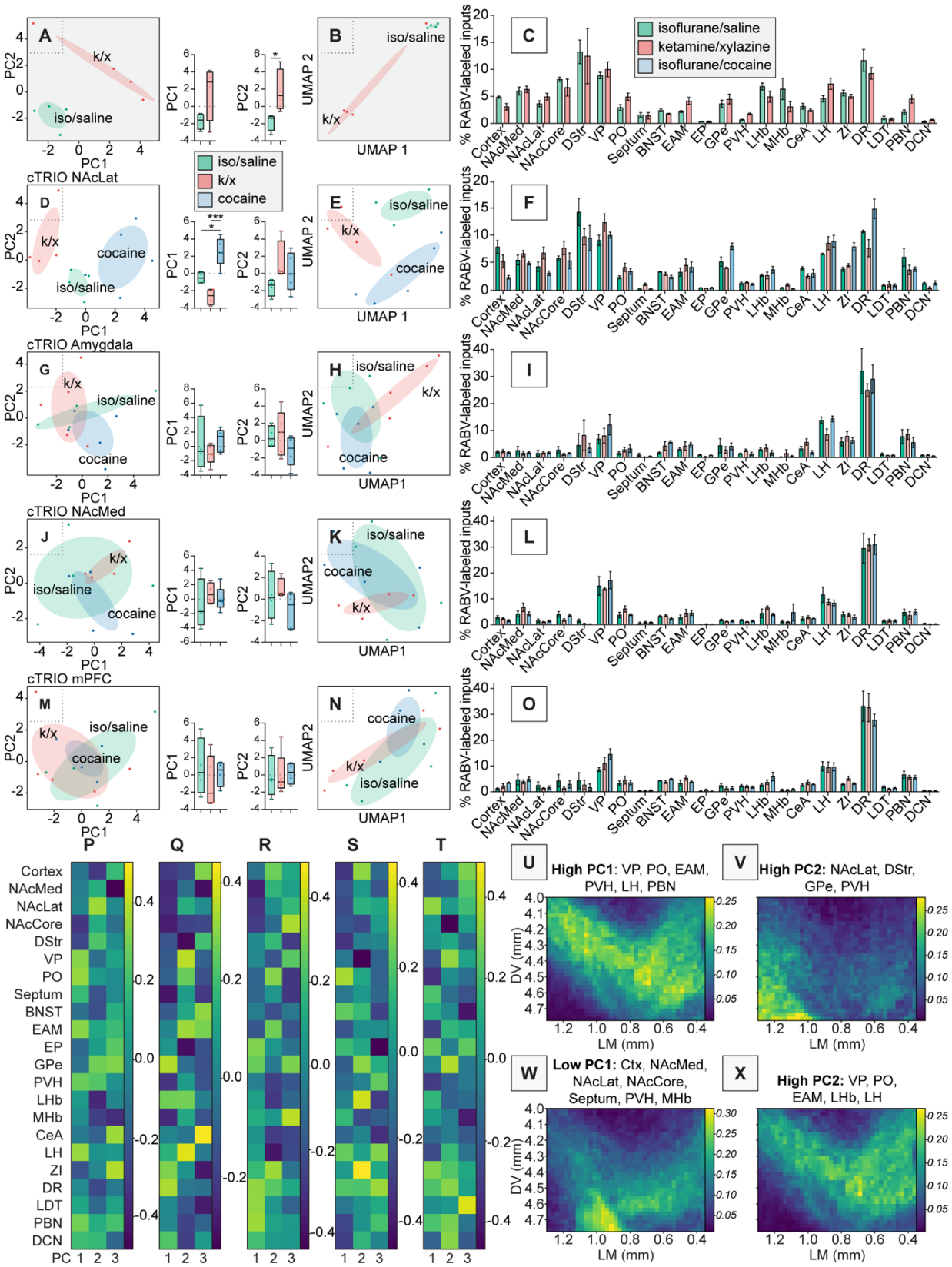
A
B
C
D
E
F
G
H
I
J
K
L
M
N
O
P
Q
R
S
T
U
V
W
X
cTRIO NAcLat
cTRIO Amygdala
cTRIO NAcMed
cTRIO mPFC
k/x
iso/saline
cocaine
iso/saline
k/x
cocaine
PC1
PC2
UMAP 1
UMAP 2
UMAP1
UMAP2
isoflurane/saline
ketamine/xylazine
isoflurane/cocaine
% RABV-labeled inputs
Cortex
NAcMed
NAcLat
NAcCore
DStr
VP
PO
Septum
BNST
EAM
EP
GPe
PVH
LHb
MHb
CeA
LH
ZI
DR
LDT
PBN
DCN
PC 1 2 3
High PC1: VP, PO, EAM, PVH, LH, PBN
High PC2: NAcLat, DStr, GPe, PVH
Low PC1: Ctx, NAcMed, NAcLat, NAcCore, Septum, PVH, MHb
High PC2: VP, PO, EAM, LHb, LH
DV (mm)
LM (mm)

1157

1158 **Figure 4: Dimensionality reduction analysis of brains from animals anesthetized with**
1159 **isoflurane and treated with either cocaine or saline, or anesthetized with ketamine/xylazine**
1160 **and treated with saline.**
1161 (A) PCA plot of input data from $VTA^{DA}$ cells from mice anesthetized either with isoflurane or K/X
1162 and given saline. Box plot comparisons of PC1 and PC2 are shown to the right for this plot and
1163 D, G, J, and M. PC1, p = 0.086, PC2, p = 0.037, unpaired t-tests. N = 4 for both.
1164 (B) UMAP plot of input data from $VTA^{DA}$ cells from mice anesthetized either with isoflurane or K/X
1165 and given saline.
1166 (C) Bar plot showing percent of RABV-labeled cells in each input region from mice anesthetized
1167 either with isoflurane or K/X and given saline.
1168 (D) PCA plot of RABV input mapping experiments to $VTA^{DA}$→NAcLat cells in mice anesthetized
1169 with isoflurane and given saline or cocaine, or anesthetized with K/X and given saline. PC1, One-
1170 way ANOVA p = 0.0003, pairwise t-tests saline vs. cocaine multiple comparisons adjusted p =
1171 0.011, saline vs. K/X p = 0.071, K/X vs. cocaine p = 0.0002. PC2, One-way ANOVA p = 0.16. n=4
1172 for saline and K/X, n = 5 for cocaine.
1173 (E) UMAP plot of input mapping experiments to $VTA^{DA}$→NAcLat cells.
1174 (F) Bar plot showing percent of RABV-labeled cells in each input region for cTRIO experiments
1175 from $VTA^{DA}$→NAcLat cells.
1176 (G) PCA plot of input mapping experiments to $VTA^{DA}$→Amygdala cells. PC1, One-way ANOVA p
1177 = 0.48. PC2, One-way ANOVA p = 0.30. n=4 for saline, n = 5 for K/X and cocaine.
1178 (H) UMAP plot of input mapping experiments to $VTA^{DA}$→Amygdala cells.
1179 (I) Bar plot showing percent of RABV-labeled cells in each input region for cTRIO experiments
1180 from $VTA^{DA}$→Amygdala cells.
1181 (J) PCA plot of input mapping experiments to $VTA^{DA}$→NAcMed cells. PC1, One-way ANOVA p =
1182 0.64. PC2, One-way ANOVA p = 0.27. n=4 for saline and K/X, n = 5 for cocaine.
1183 (K) UMAP plot of input mapping experiments to $VTA^{DA}$→NAcMed cells.
1184 (L) Bar plot showing percent of RABV-labeled cells in each input region for cTRIO experiments
1185 from $VTA^{DA}$→NAcMed cells.
1186 (M) PCA plot of input mapping experiments to $VTA^{DA}$→mPFC cells. PC1, One-way ANOVA p =
1187 0.67. PC2, One-way ANOVA p = 0.97. n=4 for saline and cocaine, n = 5 for K/X.
1188 (N) UMAP plot of input mapping experiments to $VTA^{DA}$→mPFC cells.
1189 (O) Bar plot showing percent of RABV-labeled cells in each input region for cTRIO experiments
1190 from $VTA^{DA}$→mPFC cells.

1191 (P-T) Heatmap of the contributions of each brain region to PC1 to PC3 for data shown in (P) panel
1192 A, (Q) panel D, (R) panel G, (S) panel J, (T) panel M.
1193 (U) Projection portrait of regions with high PC1 contributions in all $VTA^{DA}$ cells: VP, PO, EAM,
1194 PVH, LH, PBN.
1195 (V) Projection portrait of regions with high PC2 contributions in $VTA^{DA}$ cells: NAcLat, DStr, GPe,
1196 PVH.
1197 (W) Projection portrait of regions with low PC1 contributions in $VTA^{DA}$→NAcLat cells: cortex,
1198 NAcMed, NAcLat, NAcCore, septum, PVH, MHb.
1199 (X) Projection portrait of regions with high PC2 contributions in $VTA^{DA}$→NAcLat cells: VP, PO,
1200 EAM, LHb, LH.

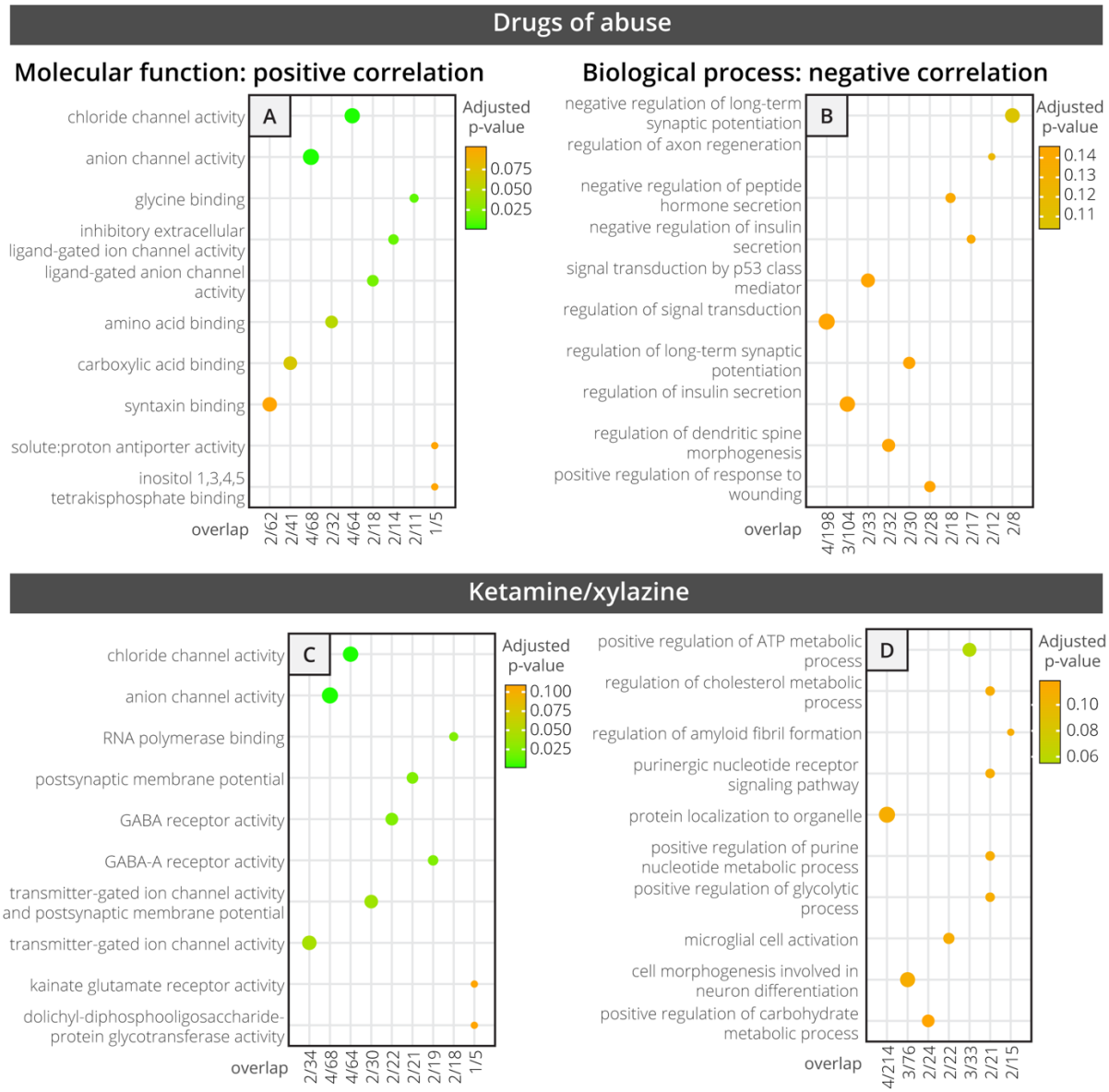


**Figure 5: Gene ontology (GO) analysis of top 50 genes within the Allen Gene Expression Atlas correlated with differences in RABV input labeling obtained from experimental vs. control mice**.

(A-B) GO from an average of the addictive drug conditions vs. saline-treated controls, all anesthetized using isoflurane.

(C-D) GO from K/X-anesthetized vs. isoflurane-anesthetized saline-treated mice.

Panels A and C show molecular function-related gene classes whose expression was positively correlated with RABV labeling differences, and panels B and D show GO analyses that reflect biological process-related gene classes whose expression was negatively correlated with RABV labeling differences.

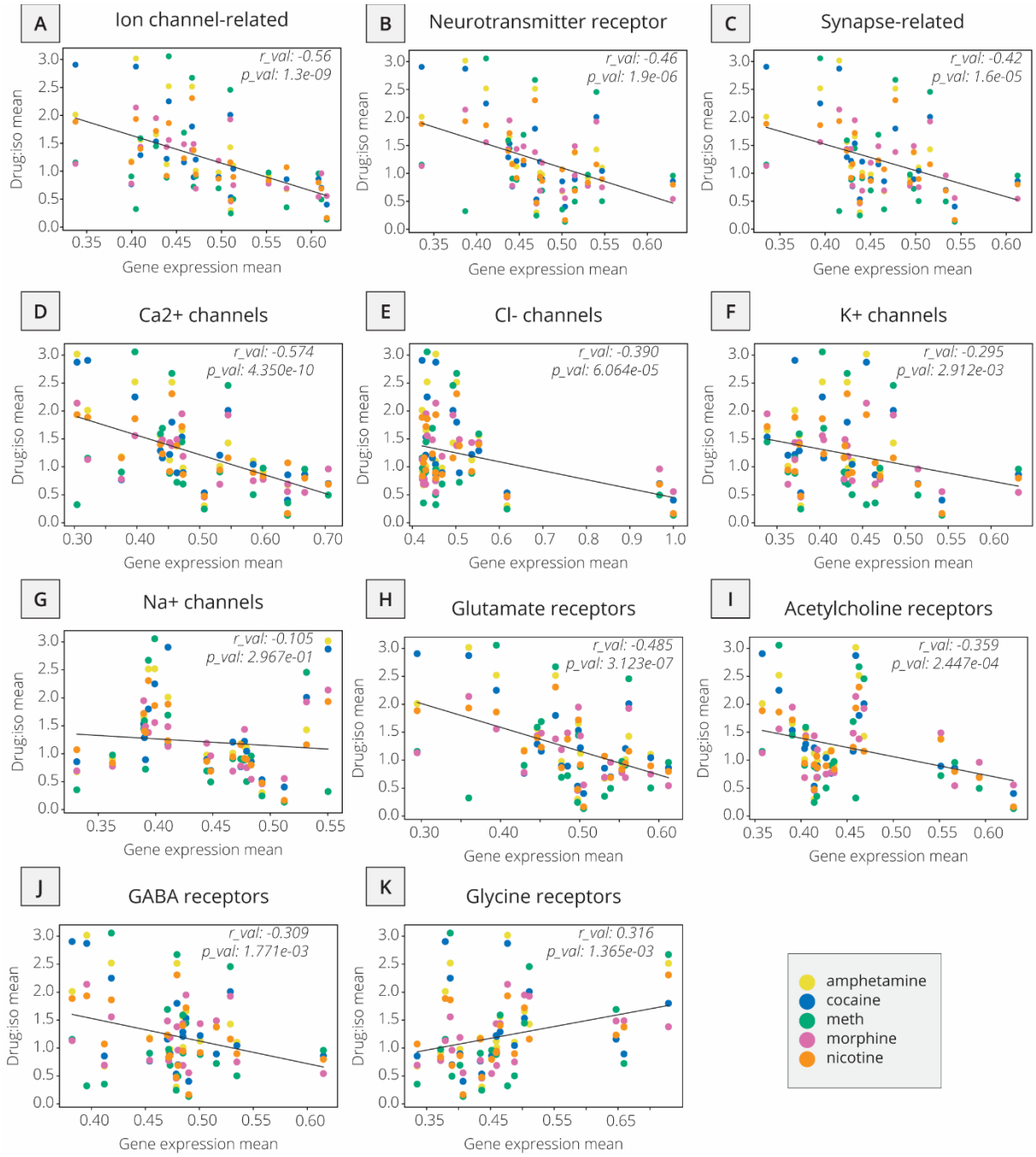


**Figure 6: Relationship between RABV labeling ratio in addictive drug/saline-treated groups and mean basal gene expression of gene subgroups, subtypes of ion channels, and neurotransmitter receptors.** Linear regressions are shown for all five examined drugs against different gene classes expressed by brain region within the Allen Gene Expression Atlas, including (A) ion channel-related genes, (B) neurotransmitter-related genes, (C) synapse-related genes, (D) $Ca^{2+}$ channels, (E) $Cl^{-}$ channels, (F) $K^{+}$ channels, (G) $Na^{+}$ channels, (H) glutamate receptors, (I) acetylcholine receptors, (J) GABA receptors, (K) glycine receptors.

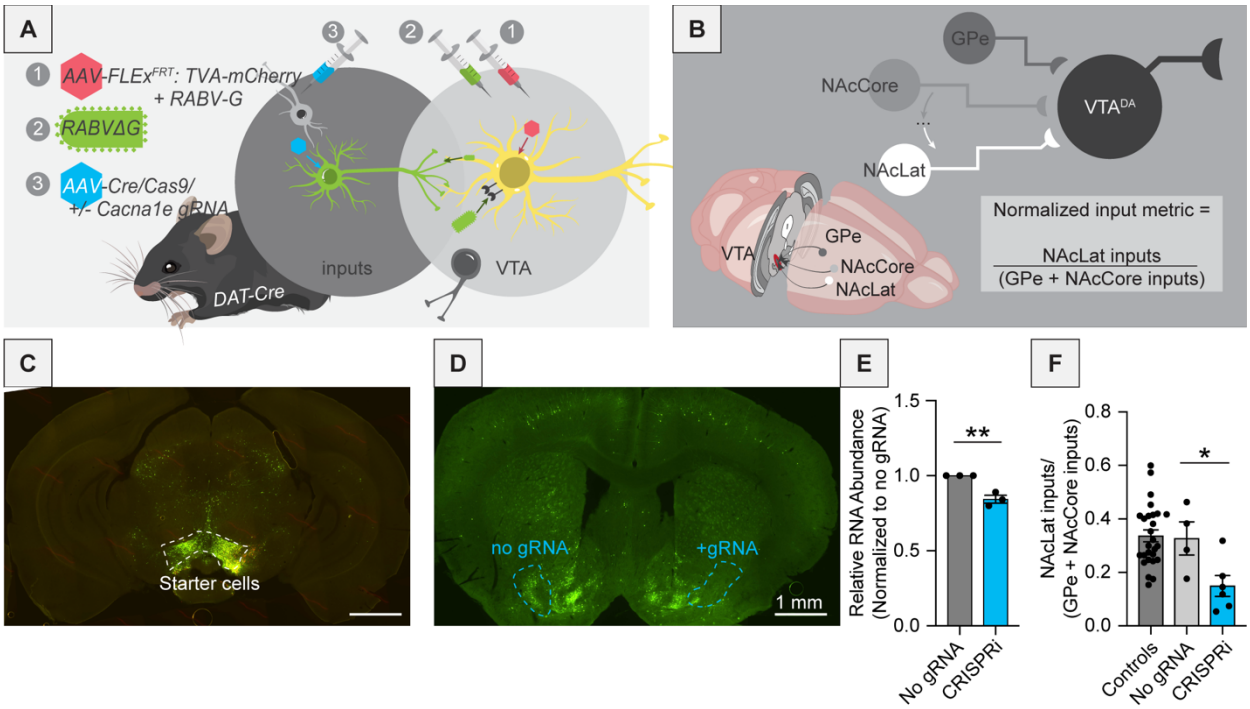


**Figure 7: Inhibition of *Cacna1e* expression in the NAcLat reduces RABV-labeled inputs from the NAcLat onto VTA$^{DA}$ cells.**

(A) Schematic of viral injections performed.

(B) Schematic of connectivity in relevant brain regions and explanation of the normalized input metric.

(C) Representative image of fluorescence in starter cells in the VTA. Scale, 1 mm.

(D) Representative image of fluorescence in the NAcLat after either administration of no gRNA (left) or gRNA targeting *Cacna1e* (right). Scale, 1 mm.

(E) qPCR results showing slight inhibition of *Cacna1e* in the NAcLat.

(F) Difference in RABV-labeled inputs after CRISPRi-mediated knockdown of *Cacna1e* compared to controls[15], and no gRNA.

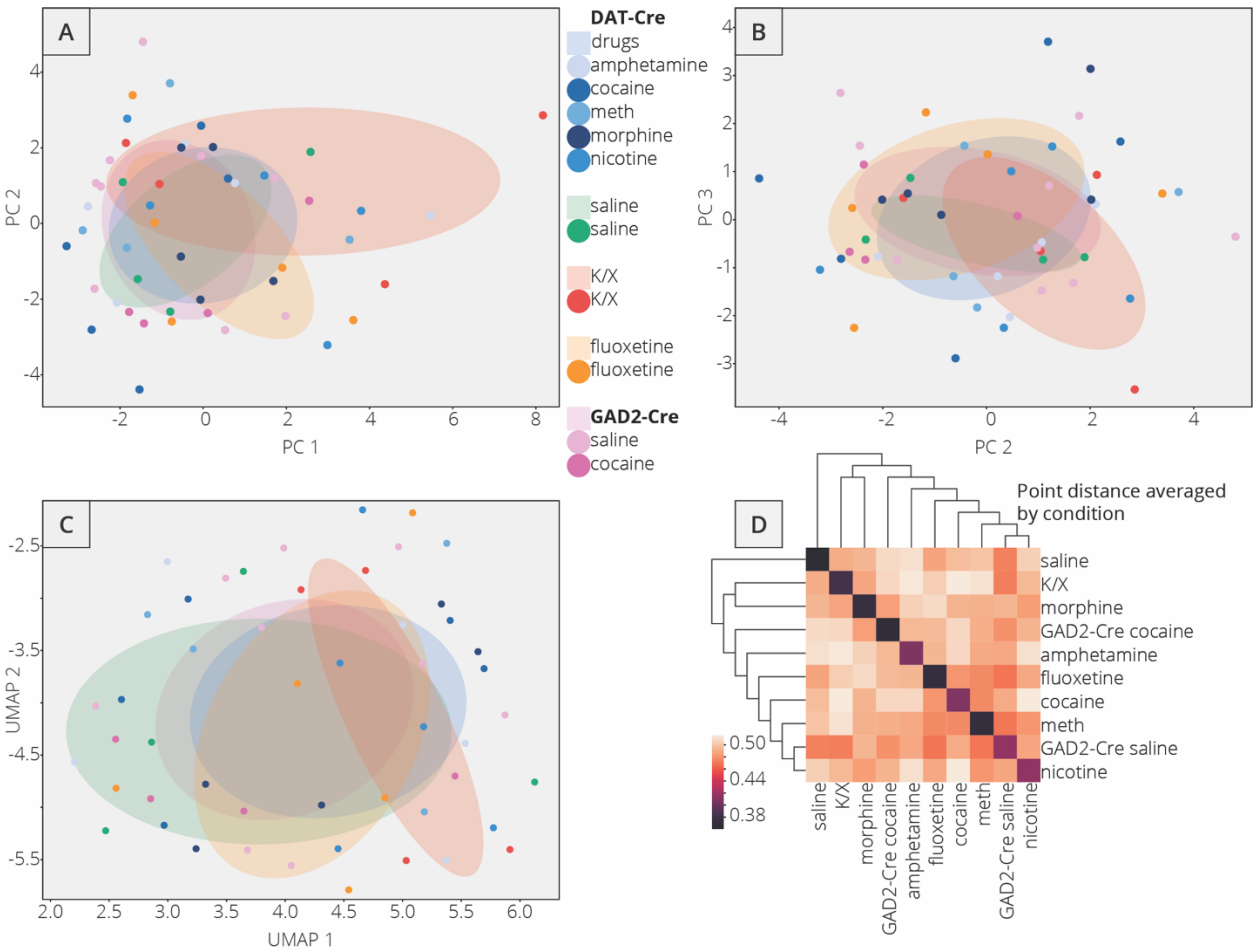


**Figure S1: Brains from animals treated with a single exposure to a drug (Figure 3A), but with the brain identities scrambled.**

(A) PCA plot showing the data with scrambled identities along PC1 and PC2.

(B) The same scrambled data along PC1 and PC3.

(C) UMAP of the scrambled data.

(D) Correlogram of 20 UMAP embeddings of the scrambled data.

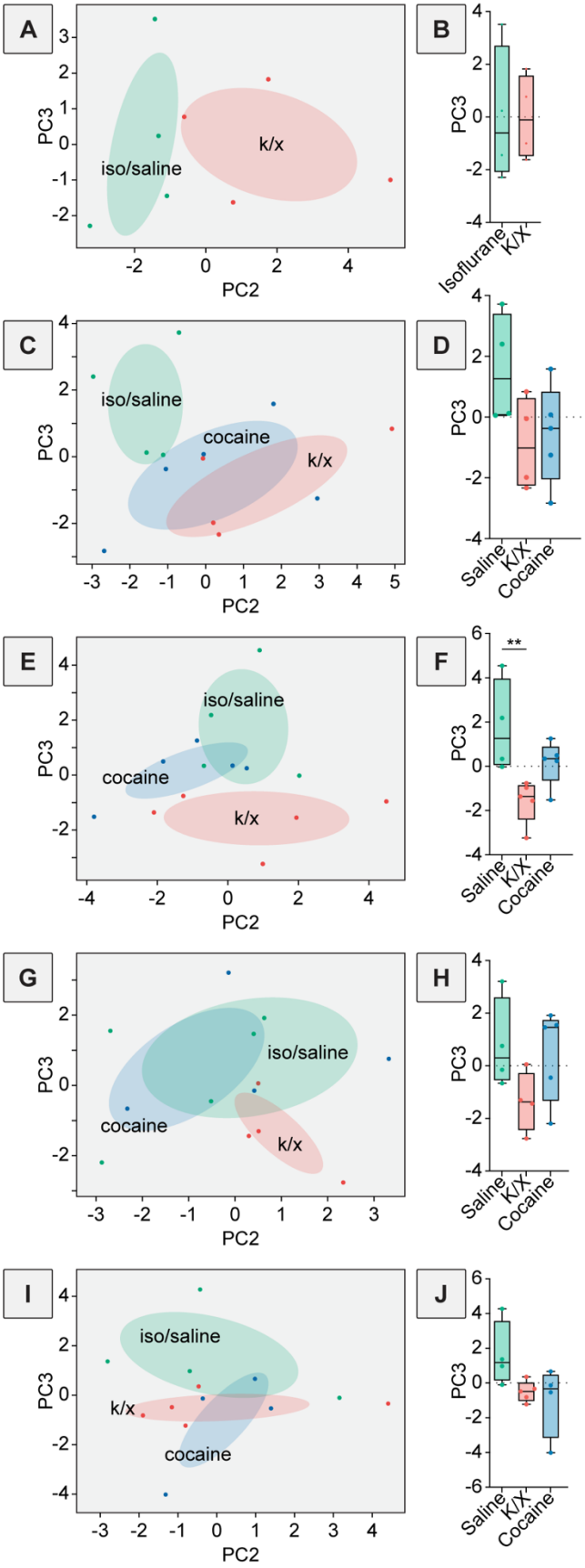
A
B
C
D
E
F
G
H
I
J
PC2
PC3
iso/saline
k/x
cocaine
Isoflurane
Saline
Cocaine
**

1239

1240 **Figure S2: Dimensionality reduction analysis of brains from animals anesthetized with**
1241 **isoflurane and treated with either cocaine or saline, or anesthetized with ketamine/xylazine**
1242 **and treated with saline, focusing on PC3.**
1243 (A) PCA plot of input data from $VTA^{DA}$ cells from mice anesthetized either with isoflurane or K/X
1244 and given saline, showing PC2 and PC3.
1245 (B) Box plot comparisons of PC3, p = 0.99, unpaired t-tests. N = 4 for both.
1246 (C) PCA plot of RABV input mapping experiments to $VTA^{DA}$→NAcLat cells in mice anesthetized
1247 with isoflurane and given saline or cocaine, or anesthetized with K/X and given saline, showing
1248 PC2 and PC3.
1249 (D) Box plot comparisons of PC3, One-way ANOVA p = 0.12. n=4 for saline and K/X, n = 5 for
1250 cocaine.
1251 (E) PCA plot of input mapping experiments to $VTA^{DA}$→Amygdala cells, showing PC2 and PC3.
1252 (F) Box plot comparisons of PC3, PC1, One-way ANOVA p = 0.014, pairwise t-tests saline vs.
1253 K/X multiple comparisons adjusted p = 0.011, saline vs. cocaine p = 0.24, K/X vs. cocaine p =
1254 0.16. n=4 for saline, n = 5 for K/X and cocaine.
1255 (G) PCA plot of input mapping experiments to $VTA^{DA}$→NAcMed cells, showing PC2 and PC3.
1256 (H) Box plot comparisons of PC3,, One-way ANOVA p = 0.64. PC2, One-way ANOVA p = 0.16.
1257 n=4 for saline and K/X, n = 5 for cocaine.
1258 (I) PCA plot of input mapping experiments to $VTA^{DA}$→mPFC cells, showing PC2 and PC3.
1259 (J) Box plot comparisons of PC3, One-way ANOVA p = 0.67. PC2, One-way ANOVA p = 0.083.
1260 n=4 for saline and cocaine, n = 5 for K/X.
1261

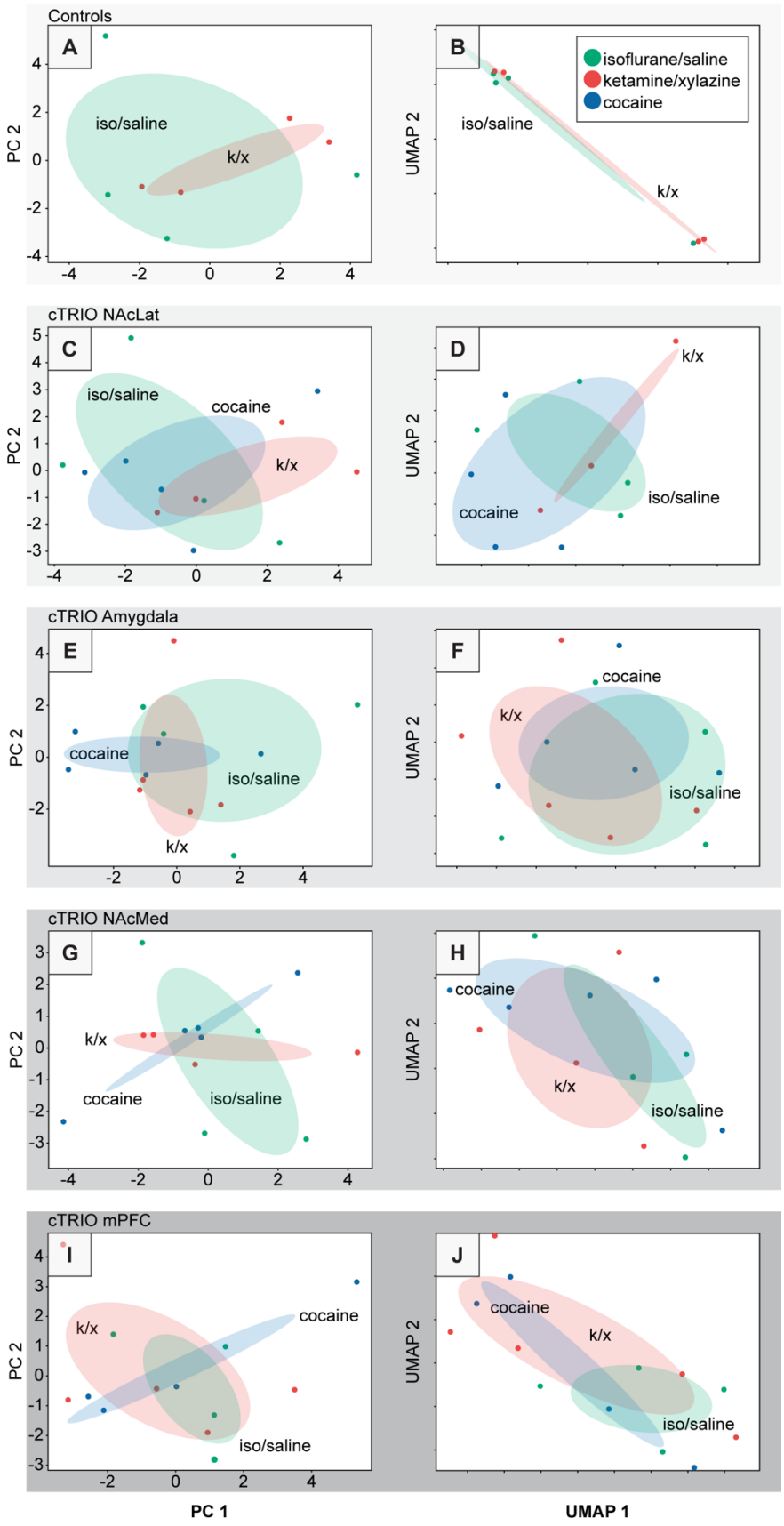
Controls
A
B
isoflurane/saline
ketamine/xylazine
cocaine
iso/saline
k/x
cTRIO NAcLat
C
D
cocaine
cTRIO Amygdala
E
F
cTRIO NAcMed
G
H
cTRIO mPFC
I
J
PC 2
UMAP 2
PC 1
UMAP 1

1262

1263 **Figure S3: Inputs to brains of mice anesthetized with isoflurane and receiving saline or**
1264 **cocaine, or K/X-saline (Figure 4), but with the brain identities scrambled.**
1265 (A) PCA plot of scrambled data from isoflurane-anesthetized and K/X-anesthetized mice.
1266 (B) UMAP plot of scrambled data from isoflurane-anesthetized and K/X-anesthetized mice.
1267 (C) PCA plot of scrambled data from input mapping experiments to $VTA^{DA}$→NAcLat cells.
1268 (D) UMAP plot of scrambled data from input mapping experiments to $VTA^{DA}$→NAcLat cells.
1269 (E) PCA plot of scrambled data from input mapping experiments to $VTA^{DA}$→Amygdala cells.
1270 (F) UMAP plot of scrambled data from input mapping experiments to $VTA^{DA}$→Amygdala cells.
1271 (G) PCA plot of scrambled data from input mapping experiments to $VTA^{DA}$→NAcMed cells.
1272 (H) UMAP plot of scrambled data from input mapping experiments to $VTA^{DA}$→NAcMed cells.
1273 (I) PCA plot of scrambled data from input mapping experiments to $VTA^{DA}$→mPFC cells.
1274 (J) UMAP plot of scrambled data from input mapping experiments to $VTA^{DA}$→mPFC cells.

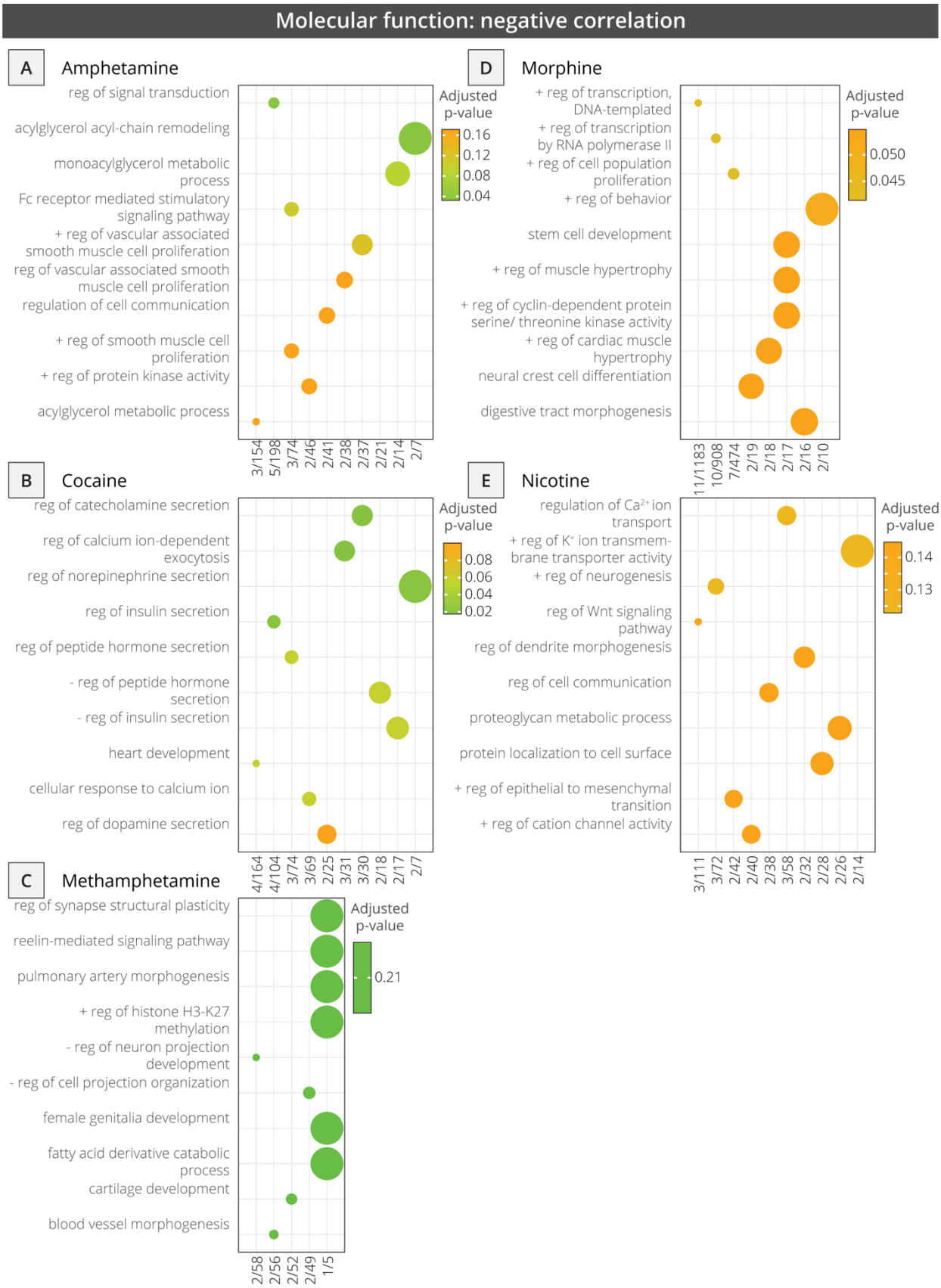
Molecular function: negative correlation
A
Amphetamine
reg of signal transduction
acylglycerol acyl-chain remodeling
monoacylglycerol metabolic process
Fc receptor mediated stimulatory signaling pathway
+ reg of vascular associated smooth muscle cell proliferation
reg of vascular associated smooth muscle cell proliferation
regulation of cell communication
+ reg of smooth muscle cell proliferation
+ reg of protein kinase activity
acylglycerol metabolic process
3/154
5/198
3/74
2/46
2/41
2/38
2/37
2/21
2/14
2/7
Adjusted p-value
0.16
0.12
0.08
0.04
B
Cocaine
reg of catecholamine secretion
reg of calcium ion-dependent exocytosis
reg of norepinephrine secretion
reg of insulin secretion
reg of peptide hormone secretion
- reg of peptide hormone secretion
- reg of insulin secretion
heart development
cellular response to calcium ion
reg of dopamine secretion
4/164
4/104
3/74
3/69
2/25
3/31
3/30
2/18
2/17
2/7
Adjusted p-value
0.08
0.06
0.04
0.02
C
Methamphetamine
reg of synapse structural plasticity
reelin-mediated signaling pathway
pulmonary artery morphogenesis
+ reg of histone H3-K27 methylation
- reg of neuron projection development
- reg of cell projection organization
female genitalia development
fatty acid derivative catabolic process
cartilage development
blood vessel morphogenesis
2/58
2/56
2/52
2/49
1/5
Adjusted p-value
0.21
D
Morphine
+ reg of transcription, DNA-templated
+ reg of transcription by RNA polymerase II
+ reg of cell population proliferation
+ reg of behavior
stem cell development
+ reg of muscle hypertrophy
+ reg of cyclin-dependent protein serine/ threonine kinase activity
+ reg of cardiac muscle hypertrophy
neural crest cell differentiation
digestive tract morphogenesis
11/1183
10/908
7/474
2/19
2/18
2/17
2/16
2/10
Adjusted p-value
0.050
0.045
E
Nicotine
regulation of Ca2+ ion transport
+ reg of K+ ion transmembrane transporter activity
+ reg of neurogenesis
reg of Wnt signaling pathway
reg of dendrite morphogenesis
reg of cell communication
proteoglycan metabolic process
protein localization to cell surface
+ reg of epithelial to mesenchymal transition
+ reg of cation channel activity
3/111
3/72
2/42
2/40
2/38
3/58
2/32
2/28
2/26
2/14
Adjusted p-value
0.14
0.13

1275

1276 **Figure S4: Gene ontology analysis of top 50 expressed genes correlated to differences in**
1277 **RABV input labeling obtained from drug-treated vs. control mice**. GO from mice treated with
1278 (A) amphetamine, (B) cocaine, (C) methamphetamine, (D) morphine, and (E) nicotine-treated
1279 relative to saline-injected controls are shown. Each GO analysis reflects molecular function-
1280 related gene classes whose expression was negatively correlated with RABV labeling differences.

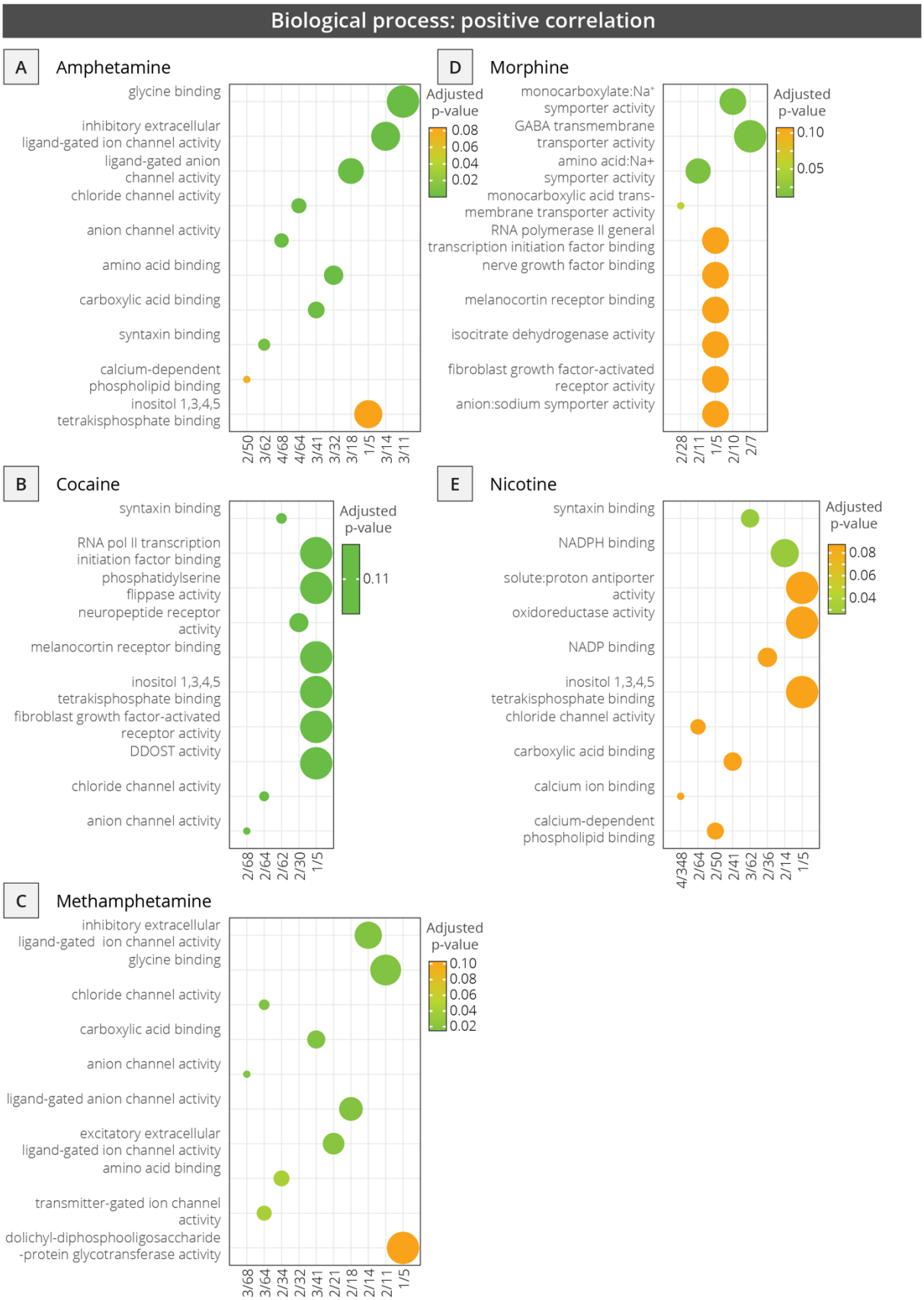
Biological process: positive correlation
A
Amphetamine
glycine binding
inhibitory extracellular ligand-gated ion channel activity
ligand-gated anion channel activity
chloride channel activity
anion channel activity
amino acid binding
carboxylic acid binding
syntaxin binding
calcium-dependent phospholipid binding
inositol 1,3,4,5 tetrakisphosphate binding
2/50 3/62 4/68 4/64 3/41 3/32 3/18 1/5 3/14 3/11
Adjusted p-value
0.08
0.06
0.04
0.02
B
Cocaine
syntaxin binding
RNA pol II transcription initiation factor binding
phosphatidylserine flippase activity
neuropeptide receptor activity
melanocortin receptor binding
inositol 1,3,4,5 tetrakisphosphate binding
fibroblast growth factor-activated receptor activity
DDOST activity
chloride channel activity
anion channel activity
2/68 2/64 2/62 2/30 1/5
Adjusted p-value
0.11
C
Methamphetamine
inhibitory extracellular ligand-gated ion channel activity
glycine binding
chloride channel activity
carboxylic acid binding
anion channel activity
ligand-gated anion channel activity
excitatory extracellular ligand-gated ion channel activity
amino acid binding
transmitter-gated ion channel activity
dolichyl-diphosphooligosaccharide -protein glycotransferase activity
3/68 3/64 2/34 2/32 3/41 2/21 2/18 2/14 2/11 1/5
Adjusted p-value
0.10
0.08
0.06
0.04
0.02
D
Morphine
monocarboxylate:Na+ symporter activity
GABA transmembrane transporter activity
amino acid:Na+ symporter activity
monocarboxylic acid trans-membrane transporter activity
RNA polymerase II general transcription initiation factor binding
nerve growth factor binding
melanocortin receptor binding
isocitrate dehydrogenase activity
fibroblast growth factor-activated receptor activity
anion:sodium symporter activity
2/28 2/11 1/5 2/10 2/7
Adjusted p-value
0.10
0.05
E
Nicotine
syntaxin binding
NADPH binding
solute:proton antiporter activity
oxidoreductase activity
NADP binding
inositol 1,3,4,5 tetrakisphosphate binding
chloride channel activity
carboxylic acid binding
calcium ion binding
calcium-dependent phospholipid binding
4/348 2/64 2/50 2/41 3/62 2/36 2/14 1/5
Adjusted p-value
0.08
0.06
0.04

1281

1282 **Figure S5: Gene ontology analysis of top 50 expressed genes correlated to differences in**
1283 **RABV input labeling obtained from drug-treated vs. control mice**. GO analyses from mice
1284 treated with (A) amphetamine, (B) cocaine, (C) methamphetamine, (D) morphine, and (E)
1285 nicotine-treated relative to saline-injected controls are shown. Each GO analysis reflects
1286 biological process-related gene classes whose expression was positively correlated with RABV
1287 labeling differences.

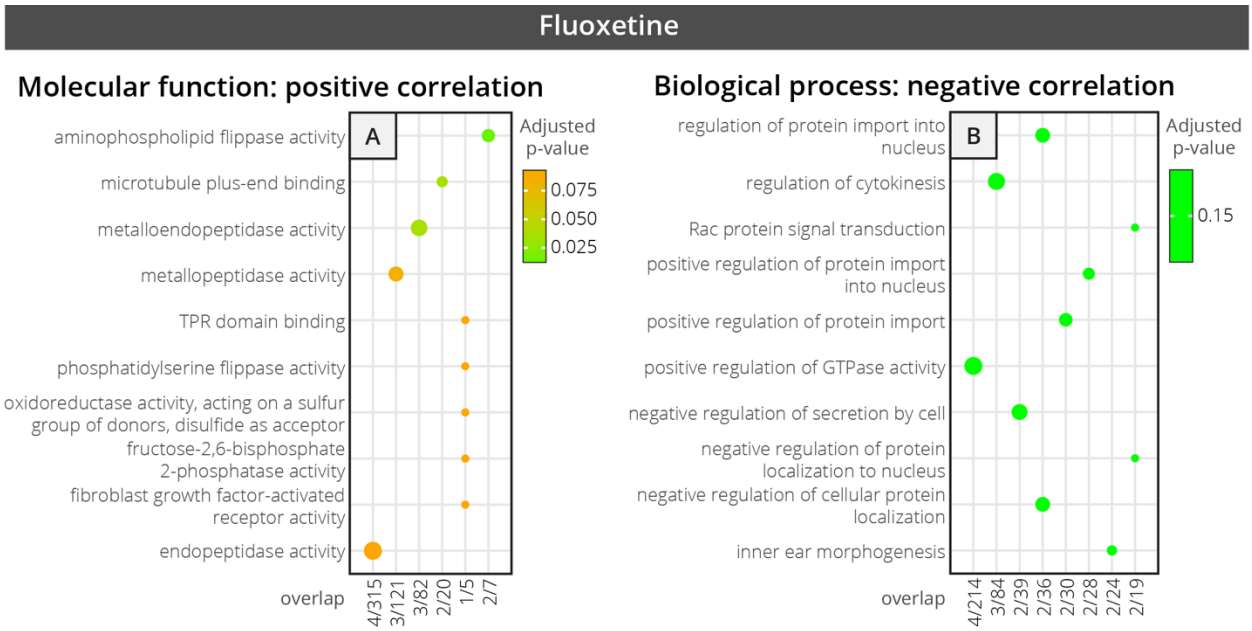


**Figure S6: Gene ontology analysis of the top 50 genes correlated with differences in RABV input labeling obtained from fluoxetine vs. saline-treated controls**. Panel (A) shows molecular function-related gene classes whose expression was positively correlated with RABV labeling differences, and panel (B) shows GO analyses that reflect biological process-related gene classes whose expression was negatively correlated with RABV labeling differences.

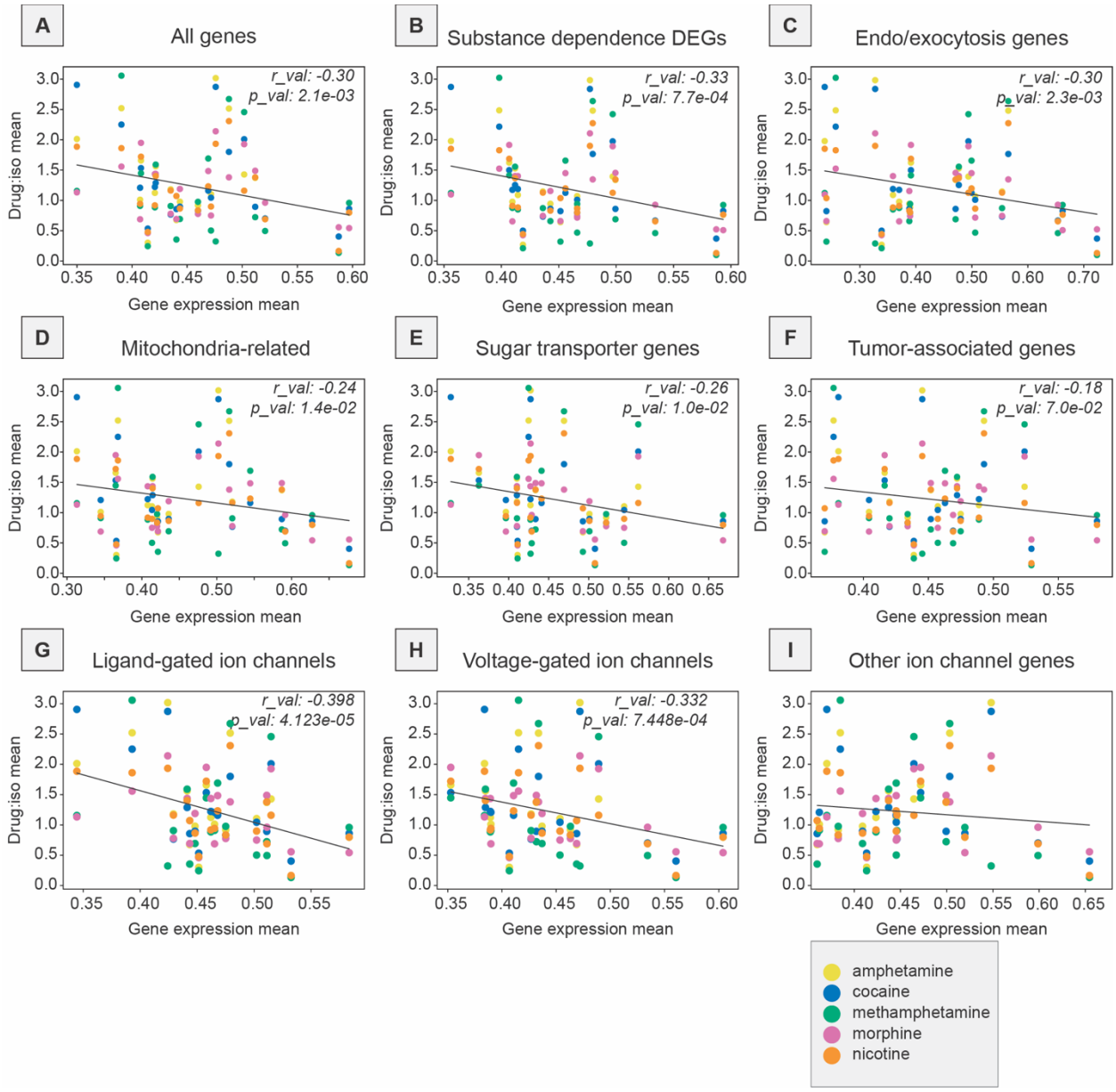


**Figure S7: Relationship between RABV labeling ratio in addictive drug/saline-treated groups and mean basal gene expression of gene subgroups.** Linear regressions are shown for all five examined drugs against all genes and different gene classes expressed by brain region within the Allen Gene Expression Atlas, including (A) all genes, (B) substance dependence-related genes, (C) endocytosis- and exocytosis-related genes, (D) mitochondrial genes, (E) sugar transporter genes, (F) tumor-associated genes, (G) ligand-gated ion channel genes, (H) voltage-gated ion channel genes, (I) other ion channel genes.

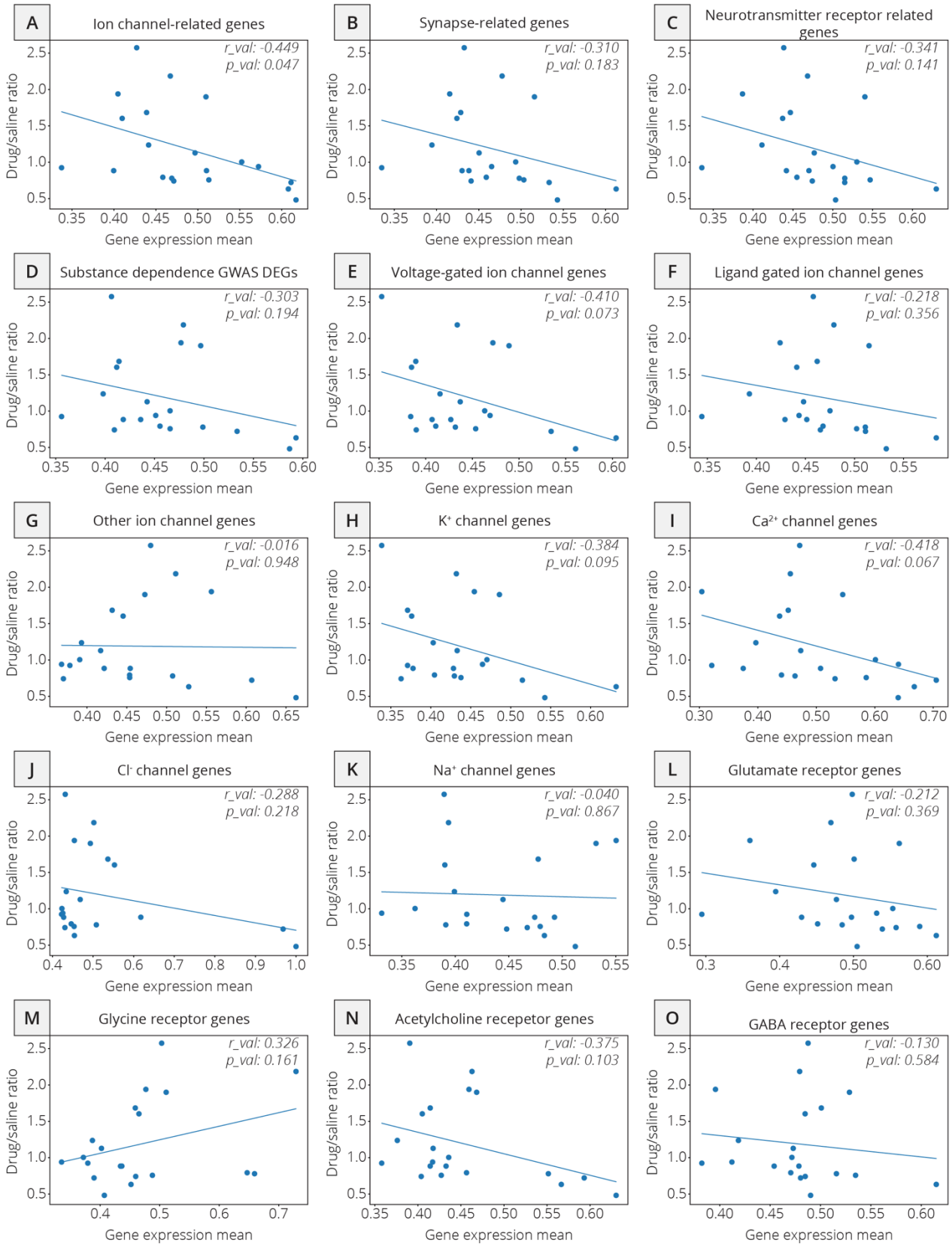
A
Ion channel-related genes
r_val: -0.449
p_val: 0.047
B
Synapse-related genes
r_val: -0.310
p_val: 0.183
C
Neurotransmitter receptor related genes
r_val: -0.341
p_val: 0.141
D
Substance dependence GWAS DEGs
r_val: -0.303
p_val: 0.194
E
Voltage-gated ion channel genes
r_val: -0.410
p_val: 0.073
F
Ligand gated ion channel genes
r_val: -0.218
p_val: 0.356
G
Other ion channel genes
r_val: -0.016
p_val: 0.948
H
K⁺ channel genes
r_val: -0.384
p_val: 0.095
I
Ca²⁺ channel genes
r_val: -0.418
p_val: 0.067
J
Cl⁻ channel genes
r_val: -0.288
p_val: 0.218
K
Na⁺ channel genes
r_val: -0.040
p_val: 0.867
L
Glutamate receptor genes
r_val: -0.212
p_val: 0.369
M
Glycine receptor genes
r_val: 0.326
p_val: 0.161
N
Acetylcholine recepetor genes
r_val: -0.375
p_val: 0.103
O
GABA receptor genes
r_val: -0.130
p_val: 0.584
Drug/saline ratio
Gene expression mean

1302

1303 **Figure S8: Relationship between RABV labeling ratio in K/X-saline vs. isoflurane-saline**
1304 **groups and mean basal gene expression of gene subgroups.** Linear regressions are shown
1305 for K/X-saline vs. isoflurane-saline groups against different gene classes, including (A) ion
1306 channel-related genes, (B) synapse-related genes, (C) neurotransmitter-related genes, (D) DEGs
1307 related to substance abuse, (E) voltage-gated ion channels, (F) ligand-gated ion channels, (G)
1308 other ion channels, (H) $K^+$ channels, (I) $Ca^{2+}$ channels, (J) $Cl^-$ channels, (K) $Na^+$ channels, (L)
1309 glutamate receptors, (M) glycine receptors, (N) acetylcholine receptors, (O) GABA receptor genes.

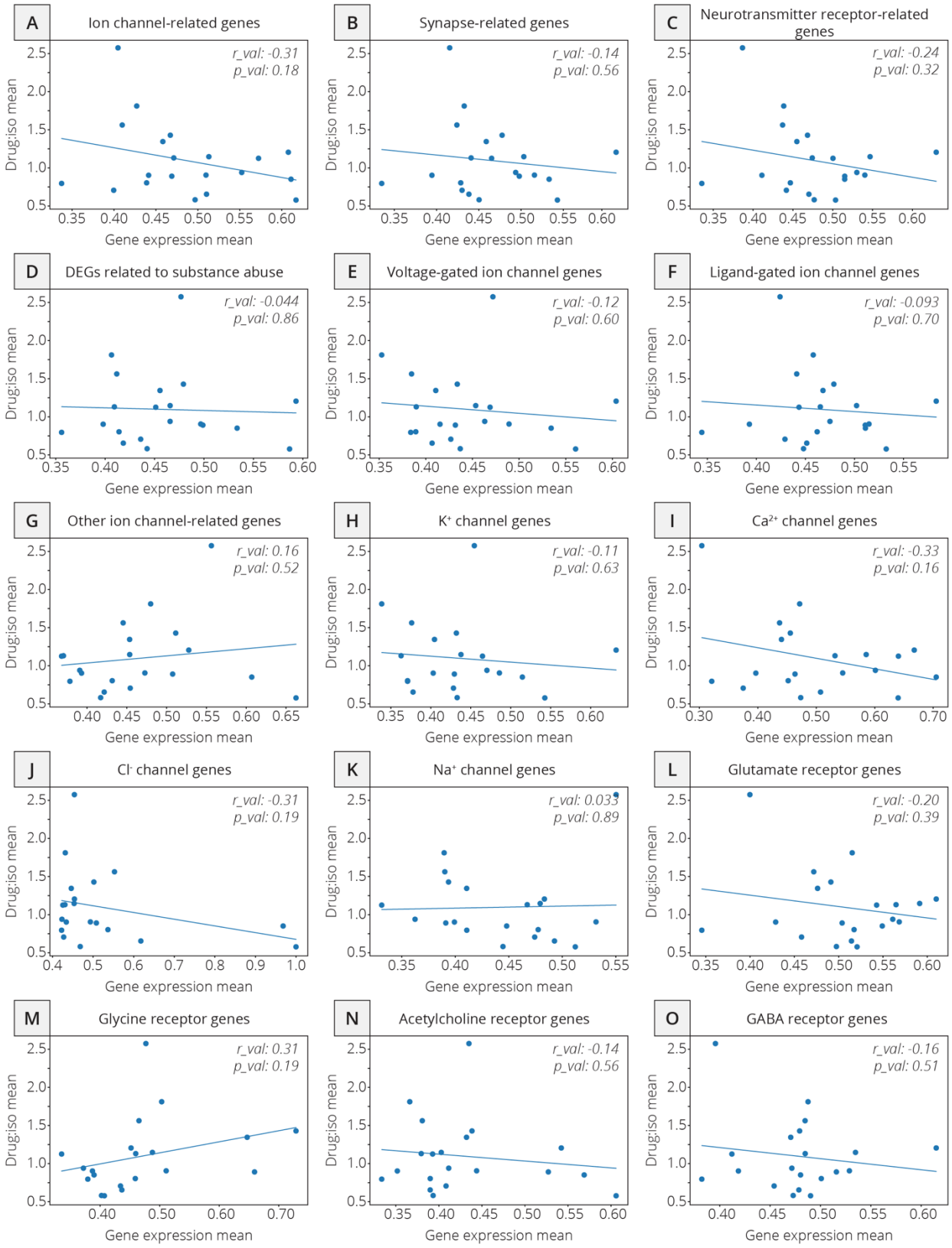
A
Ion channel-related genes
r_val: -0.31
p_val: 0.18
B
Synapse-related genes
r_val: -0.14
p_val: 0.56
C
Neurotransmitter receptor-related genes
r_val: -0.24
p_val: 0.32
D
DEGs related to substance abuse
r_val: -0.044
p_val: 0.86
E
Voltage-gated ion channel genes
r_val: -0.12
p_val: 0.60
F
Ligand-gated ion channel genes
r_val: -0.093
p_val: 0.70
G
Other ion channel-related genes
r_val: 0.16
p_val: 0.52
H
K⁺ channel genes
r_val: -0.11
p_val: 0.63
I
Ca²⁺ channel genes
r_val: -0.33
p_val: 0.16
J
Cl⁻ channel genes
r_val: -0.31
p_val: 0.19
K
Na⁺ channel genes
r_val: 0.033
p_val: 0.89
L
Glutamate receptor genes
r_val: -0.20
p_val: 0.39
M
Glycine receptor genes
r_val: 0.31
p_val: 0.19
N
Acetylcholine receptor genes
r_val: -0.14
p_val: 0.56
O
GABA receptor genes
r_val: -0.16
p_val: 0.51
Drug:iso mean
Gene expression mean

1310

1311 **Figure S9: Relationship between RABV ratio labeling in fluoxetine vs. saline-treated**
1312 **groups, both anesthetized with isoflurane, and mean basal gene expression of gene**
1313 **subgroups.** Linear regressions are shown for fluoxetine/saline-treated groups against different
1314 gene classes, including (A) ion channel-related genes, (B) synapse-related genes, (C)
1315 neurotransmitter-related genes, (D) DEGs related to substance abuse, (E) voltage-gated ion
1316 channels, (F) ligand-gated ion channels, (G) other ion channels, (H) $K^+$ channels, (I) $Ca^{2+}$
1317 channels, (J) $Cl^-$ channels, (K) $Na^+$ channels, (L) glutamate receptors, (M) glycine receptors, (N)
1318 acetylcholine receptors, (O) GABA receptor genes.